Accounting for spatial distribution in mean-field homogenization of particulate composites

Oscar Luis Cruz-González, Rémi Cornaggia, Sophie Dartois, Renald Brenner

Accounting for spatial distribution in mean-field homogenization of particulate composites.

O.L. Cruz-González[a], R. Cornaggia[b,*], S. Dartois[b], R. Brenner[b]

[a] *IRPHE Aix Marseille Univ, CNRS, Centrale Marseille, IRPHE UMR 7342, Marseille, France*
[b] *Sorbonne Université, CNRS, Institut Jean Le Rond d'Alembert, F-75005 Paris, France*

Abstract

Several mean-fields homogenization methods are readily available to estimate the effective properties of particulate composites, which take into consideration the particles volume fraction, shapes and orientations. Some of them also account for the spatial distribution of the particles. For instance, the Ponte-Castañeda and Willis (PCW) model embeds a parametrization of the global distribution law, while the Interaction Direct Derivative (IDD) model associates a matrix cell to each inclusion, that should be representative of close interactions. In the literature, IDD is commonly reduced to the particular case of the classical Mori and Tanaka (MT) scheme or to the aforementioned PCW model, and therefore, the application of its most general form is somehow lacking. In addition, spatial distribution laws used within the PCW model, are, in many cases, specified separately from the microstructural configurations. On this basis, the present study proposes a novel approach to calibrate and exploit IDD and PCW models in 2D linear conductive composite materials, provided that a representative image of the microstructure is available. We discuss the links between the models and the range of validity of the IDD model by addressing its possible lack of symmetry. In particular, when IDD is not applicable, both an IDD-based PCW model and a two-step scheme are proposed. Finally, an image analysis method using Voronoï diagrams, inspired by an original proposition by Du and Zheng (Acta Mechanica, 2002, 157, 61-80), is implemented to define the cells associated to each inclusion and supply the models. The method is validated by comparisons between the obtained IDD and PCW estimates, the MT model and benchmark full-field (FF) numerical simulations. Possible extensions to realistic elastic composites are discussed.

Preprint submitted to Journal of the Mechanics and Physics of Solids *October 3, 2023*

*Corresponding author
Email address: remi.cornaggia@sorbonne-universite.fr (R. Cornaggia)

Keywords: microstructures, particulate reinforced material, homogenization, spatial distribution, Voronoï Diagram

1. Introduction

The ongoing development of more efficient and sustainable composite materials is a current phenomenon across multiple industries. Nowadays, a variety of composites are created with the aim of realizing a spectrum of objectives, such as weight reduction, enhanced permeability, augmented sound or thermal insulation, and amplified ductility or strength [1, 2, 3]. During this process, the effective behavior of the materials is often evaluated through homogenization methods. These methods are used to determine the macroscopic response of the material when it is exposed to external loads such as thermal or mechanical forces at a significantly larger scale, which is well separated from the microstructural scale. This approach enables to investigate the behavior of materials with varying microstructures and gain a comprehensive understanding of their mechanical and thermal properties at the macroscopic level.

In the literature, several micromechanical homogenization methods are available. On the one hand, numerical full-field approaches [4, 5, 6] provide the "exact" effective properties of specific microstructures, up to numerical approximation. As a downside, they may be computationally expensive, especially when studying the influence of microstructural variations by performing multiple evaluations. On the other hand, mean-field models are based on the estimation of average fields of interest as stresses, strains, heat flux, intensity, etc., in the constituents of the composite [7]. In the context of matrix-inclusion composites, approximating the inclusion shapes by ellipsoids (ellipses in 2D) allows to use the Eshelby method [8] to produce such estimates. Thus, a quick calculation of the effective properties from a representative image or statistical descriptors of the microstructure can be performed.

As stated in [9], an ideal mean-field estimation scheme for the effective properties of composites should adequately account for the influence of the inclusion distribution and the interaction between inclusions and their immediately surrounding matrix. In particular, the

spatial distribution emerges as a relevant statistical descriptor of a composite, and may depend on manufacturing process parameters such as, injection speed, mixing process, etc., especially for medium and high volume fractions of fibers [10, 11]. The Mori-Tanaka (MT) model [12, 13] is a well-established approach for analyzing multi-phase composites. It incorporates the effects of inclusion interaction and is applicable for a wide range of inclusion geometries, including both isotropic and anisotropic materials. Nevertheless, the MT model does not account for the spatial distribution of inclusions. Conversely, there exist advanced mean-field models which are capable of addressing this limitation of the MT model, such as the Ponte-Casteñeda and Willis (PCW) model [14], which relies on a statistical description of the phase distribution, and micromechanical double-inclusion approaches [15] that lead to the derivation of the Interaction Direct Derivative (IDD) model [9, 16].

Based on the above, this study proposes a novel approach for calibrating and utilizing IDD and PCW models in the homogenization of two-dimensional (2D) linear conductive composite materials. The composites consist of a matrix reinforced by elliptical inclusions, both isotropic materials. Four different modeling approaches are applied: MT, PCW, IDD, and a FFT-based full field approach (FF). While MT and FF are widely used in the literature and their parameter selection is well established, to the best of the authors' knowledge, in the case of IDD and PCW, the selection of cell parameters from a given microstructure remains unclear, despite their usage in prior studies [17, 11, 18, 19].

The aim of this work is to provide an accurate estimate of the effective behavior of conductive composite materials using the PCW and IDD approaches from a microstructure image. Moreover, the research strives to determine under which conditions these methods offer better outcomes compared to MT. FF simulations results will be used as references. It is first pointed out that the IDD estimate may lack the major symmetry. In these specific cases, an IDD-based PCW model and the two-step homogenization approach from [20] are proposed to overcome this issue. The main novelty of the paper then lies in proposing an image processing technique using Voronoï diagrams that permits the selection of cells associated to each inclusion in the IDD scheme. Additionally, the distributional cell and the

corresponding Hill polarization tensor in the PCW scheme are defined in such a way that this method directly connects to the IDD scheme, as a particular case, and also benefits from all the information coming from the Voronoï diagrams. Finally, we present our findings for a variety of artificial microstructures chosen to exhibit "distributional" effects and to underline the relevance of the presented models.

The manuscript is organized as follows. In Section 2, we give an overview of the homogenization methods in the context of the conductivity problem, where the existing links between MT, PCW and IDD models are discussed. In Section 3, we present our main proposal concerning the properties and practical implementation of the IDD model, and notably the determination of the cells representative of the spatial distribution. Section 4 describes the methods, modeling methodology and numerical tools used for the purposes of the manuscript. Then, in Section 5, we explore 3 different microstructural frameworks that hold fundamental significance, and perform comparisons between the homogenization schemes. Finally, in Section 6 we summarize our findings and discuss the limitations and possible extensions of our work. Well-known useful formula and auxiliary results are gathered in appendices for completeness.

2. Homogenization of conductive composites

Let us consider a heterogeneous, linear conductive material occupying a domain $\mathscr{B}$ (see Figure 1 (a)). Analogous to the measurement of the macroscopic properties of a material from a representative test specimen, here, it is considered a representative volume element (RVE) $\mathscr{V}$ (see Figure 1 (b)) on the microscopic level, which has to be representative of the entire material.

Focusing on matrix-inclusions composites, $\mathscr{V}_M = \mathscr{V}_0$ refers to the matrix domain and $\mathscr{V}_\mathrm{I} = \cup_{\alpha=1}^{N} \mathscr{V}_\alpha$ represent the inclusions domain with $N \in \mathbb{N}$. The interfaces between inclusions and matrix, denoted $\mathscr{I}$, are assumed to be perfect.

In the absence of heat sources, the temperature field u and the heat flux $\boldsymbol{q}$ satisfy the

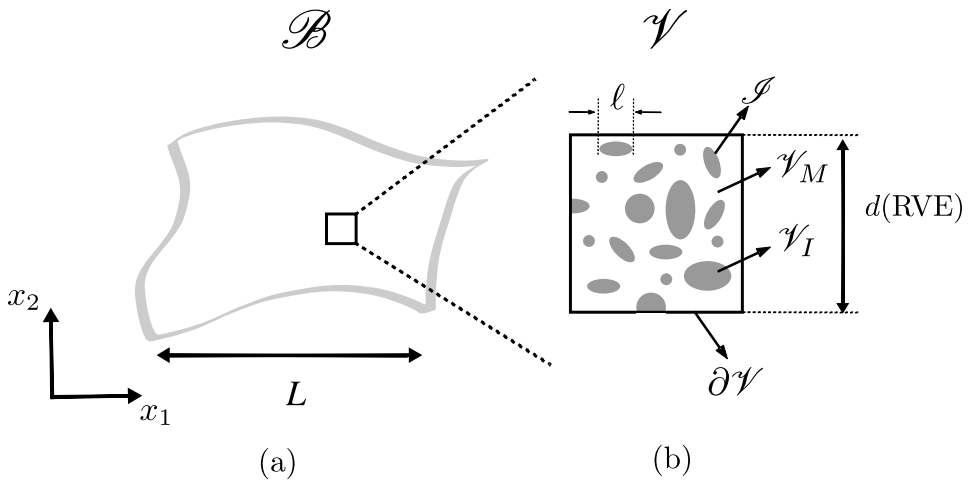

Figure 1: (a) Macroscale, (b) Microscale: representative volume element (RVE).

thermal equilibrium equation and transmission conditions across interfaces:

$$\boldsymbol{\nabla} \cdot \boldsymbol{q} = 0 \quad \text{in } \mathscr{V} \setminus \mathscr{I}, \quad [\![u]\!] = 0 \quad \text{and} \quad [\![\boldsymbol{q} \cdot \boldsymbol{n}]\!] = 0 \quad \text{on } \mathscr{I}, \tag{1}$$

where $\boldsymbol{n}$ denotes the normal vectors to the interface $\mathscr{I}$, and $[\![\cdot]\!]$ denotes the jumps across the interface $\mathscr{I}$.

Additionally, the temperature $u(\boldsymbol{x})$ is linked to the heat flux $\boldsymbol{q}(\boldsymbol{x})$ by Fourier's law,

$$\boldsymbol{q}(\boldsymbol{x}) = -\boldsymbol{k}(\boldsymbol{x})\boldsymbol{g}(\boldsymbol{x}), \tag{2}$$

where $\boldsymbol{g}(\boldsymbol{x}) := \nabla u(\boldsymbol{x})$ represents the local intensity field, and $\boldsymbol{k}(\boldsymbol{x})$ refers to the second-order conductivity tensor which is symmetric and positive definite.

The macro-heat flux $\langle \boldsymbol{q} \rangle$ and macro-intensity $\langle \boldsymbol{g} \rangle$ which characterize the state of the material at the macroscopic level are defined as the averages of their microscopic counterparts in the RVE, that is,

$$\langle \boldsymbol{q} \rangle := \frac{1}{|\mathscr{V}|} \int_{\mathscr{V}} \boldsymbol{q}(\boldsymbol{x}) d\mathscr{V}, \qquad \langle \boldsymbol{g} \rangle := \frac{1}{|\mathscr{V}|} \int_{\mathscr{V}} \boldsymbol{g}(\boldsymbol{x}) d\mathscr{V}. \tag{3}$$

The aim of the homogenization is to obtain the effective behavior that describes the composite at the macro scale based on the information at the micro scale, *i.e.* the constant effective conductivity tensor $\boldsymbol{k}_{\text{eff}}$ that relates the macroscopic flux and intensity as follows:

$$\langle \boldsymbol{q} \rangle = -\boldsymbol{k}_{\text{eff}} \langle \boldsymbol{g} \rangle . \tag{4}$$

This effective tensor can be computed numerically by solving elementary problems on the RVE to determine the local fields (hence the name *full-field* for this approach) for various representative load cases, as precised for completeness in Appendix A. These full-field problems can be solved using several numerical methods, *e.g.* finite elements [21, 4] or FFT-based methods [5, 6]. However (i) these computations can be costly (not in the 2D conductivity examples provided in the present paper but for instance for 3D elasticity and large RVE, or when many microstructures should be evaluated as inthe case of parametric sensitivity studies) and (ii) require a perfect knowledge of the microstructure in the RVE (*i.e.* the conductivity field $\boldsymbol{k}(\boldsymbol{x})$), while one often only has access to statistical information about a composite.

In contrast with these full-field methods, *mean-field* methods provide only estimates of the effective properties, by approximating the means of the fields in each constitutive phase for piecewise-homogeneous composites. These semi-analytical estimates are much faster to compute and thus emerge as an alternative to FF computations. They are presented now.

2.1. Mean-field homogenization

Let us consider now a multi-phase composite with piecewise constant properties, so that the conductivity field can be stated as follows:

$$\boldsymbol{k}(\boldsymbol{x}) = \sum_{\alpha=0}^{N} \boldsymbol{k}_\alpha \chi_\alpha(\boldsymbol{x}), \tag{5}$$

where $\boldsymbol{k}_\alpha$ is the conductivity tensor of the α-th phase, and $\chi_\alpha(\boldsymbol{x})$ refers to characteristic function of the domain $\mathscr{V}_\alpha$.

The aim of the mean-field methods is to obtain estimates of the mean values $\langle \boldsymbol{q} \rangle_\alpha$ and $\langle \boldsymbol{g} \rangle_\alpha$ in the different phases, given the overall means $\langle \boldsymbol{q} \rangle$ and $\langle \boldsymbol{g} \rangle$. Here, the notation $\langle \cdot \rangle_\alpha$ refers to the mean over the α-th phase, namely

$$\langle \cdot \rangle_\alpha := \frac{1}{|\mathscr{V}_\alpha|} \int_{\mathscr{V}_\alpha} (\cdot) d\mathscr{V}_\alpha, \tag{6}$$

so that $\langle \cdot \rangle = \sum_{\alpha=0} \mathsf{c}_\alpha \langle \cdot \rangle_\alpha$ and c_α is the volume fraction of the phase $\mathscr{V}_\alpha$.

Since the thermal equilibrium problem is linear, there exist the so-called second order *localization tensor* $\mathbb{A}$ and the mean tensors $\mathbb{A}_\alpha = \langle \mathbb{A} \rangle_\alpha$ that link microscopic and macroscopic quantities:

$$\boldsymbol{g}(\boldsymbol{x}) = \mathbb{A}(\boldsymbol{x}) \langle \boldsymbol{g} \rangle , \quad \text{and} \quad \langle \boldsymbol{g} \rangle_\alpha = \mathbb{A}_\alpha \langle \boldsymbol{g} \rangle . \tag{7}$$

The following property is readily fulfilled:

$$\langle \mathbb{A} \rangle = \sum_{\alpha=0}^{N} \mathsf{c}_\alpha \mathbb{A}_\alpha = \boldsymbol{I}. \tag{8}$$

At this point, if the mean localization tensors are known, one can compute the average flux as:

$$\langle \boldsymbol{q} \rangle = \sum_{\alpha=0}^{N} \mathsf{c}_\alpha \langle \boldsymbol{q} \rangle_\alpha = \sum_{\alpha=0}^{N} \mathsf{c}_\alpha (-\boldsymbol{k}_\alpha \langle \boldsymbol{g} \rangle_\alpha) = - \left(\sum_{\alpha=0}^{N} \mathsf{c}_\alpha \boldsymbol{k}_\alpha \mathbb{A}_\alpha \right) \langle \boldsymbol{g} \rangle , \tag{9}$$

and by analogy with Eq. (4), the effective conductivity is given by:

$$\boldsymbol{k}_{\text{eff}} = \sum_{\alpha=0}^{N} \mathsf{c}_\alpha \boldsymbol{k}_\alpha \mathbb{A}_\alpha = \langle \boldsymbol{k} \mathbb{A} \rangle . \tag{10}$$

Additionally, for matrix-inclusions composites, Eq. (10) is commonly rewritten in such way that it only depends on the inclusion localization tensors using the property (8) to remove the mean matrix localization tensor $\mathbb{A}_0$:

$$\boldsymbol{k}_{\text{eff}} = \boldsymbol{k}_0 + \sum_{\alpha=1}^{N} \mathsf{c}_\alpha (\boldsymbol{k}_\alpha - \boldsymbol{k}_0) \mathbb{A}_\alpha . \tag{11}$$

Finding the exact values of mean localization tensors $\mathbb{A}_\alpha$ would require to solve local equilibrium problems such as (A.1a)-(A.1d). Instead, mean-fields methods look for approximations of these tensors, using hypotheses on the phase geometries and spatial distributions.

2.2. Considered mean-field schemes

Eshelby's equivalent inclusion method was proposed by Eshelby in [8] to determine the elastic solutions of a single ellipsoidal inclusion embedded in an infinite matrix with uniform external loading. This micromechanical estimation has been the backbone of most mean-field methods. In particular, when the volume fraction of the inclusions in a composite

is very low, the interactions between the inclusions can be considered negligible and the dilute approximation arises naturally from Eshelby's theory, using the formula (11) with the inclusion localization tensor computed as if it was isolated in the matrix, namely

$$\mathbb{A}_\alpha^{(\mathrm{incl})} = \left(\boldsymbol{I} + \mathbb{P}_\alpha^{(\mathrm{incl})}(\boldsymbol{k}_\alpha - \boldsymbol{k}_0)\right)^{-1}, \tag{12}$$

where $\mathbb{P}_\alpha^{(\mathrm{incl})}$ stands for the Hill tensor of the α-th inclusion that accounts for its geometry: see [22] and Appendix B.2 for specific expressions.

The following is a brief summary of the mean-field methods of interest for the present work. We extensively rely on the formalism chosen by [11, 18] to write the effective stiffness tensors of elastic composites. Here, we adapt these expressions for the purposes of the conductivity problem.

2.2.1. Mori-Tanaka approximation

In the Mori-Tanaka scheme [12] as reformulated by Benveniste [23, 13], the field in the matrix at a sufficient distance from an inclusion is approximated by the constant value of its mean. As a result, the existence of further inclusions is encoded in the mean field of the matrix, and thus the method takes into account the particle interactions. The mean field of the inclusion in this model is linked to the mean field of the matrix by Eshelby's localization tensor (12) instead of the total mean field.

Based on these considerations, the mean localization tensor of the α-th inclusion takes the following form:

$$\mathbb{A}_\alpha^{(\mathrm{MT})} = \mathbb{A}_\alpha^{(\mathrm{incl})} \left(\mathsf{c}_0 \boldsymbol{I} + \sum_{\beta=1}^{N} \mathsf{c}_\beta \mathbb{A}_\beta^{(\mathrm{incl})} \right)^{-1}. \tag{13}$$

2.2.2. Ponte-Castañeda and Willis estimate

The Ponte Castañeda and Willis scheme was proposed in [14] to address the effective behavior of heterogeneous materials containing ellipsoidal arrangements of matrix-embedded inhomogeneities, and accounts for inclusion shape and spatial distribution independently. It is a generally applicable method that is based on the generalized Hashin-Shtrikman variational structure [24]. A distinctive feature of the scheme is the existence of a common

ellipsoidal cell that characterizes the spatial distribution of the inclusions. Readers are referred to [25] for the PCW model applied to conductive composites.

The localization tensors for this scheme is given as follows,

$$\mathbb{A}_{\alpha}^{(\mathrm{PCW})} = \mathbb{A}_{\alpha}^{(\mathrm{incl})} \left(\boldsymbol{I} - \mathbb{P}^{(\mathrm{cell})} \sum_{\beta=1}^{N} \mathsf{c}_{\beta} \left(\boldsymbol{k}_{\beta} - \boldsymbol{k}_{0} \right) \mathbb{A}_{\beta}^{(\mathrm{incl})} \right)^{-1}, \tag{14}$$

where $\mathbb{P}^{(\mathrm{cell})}$ stands for the Hill tensor of the "distributional" ellipsoid characterizing the spatial distribution, see Figure 2(b).

2.2.3. Interaction Direct Derivative model

The Interaction Direct Derivative model was introduced by Zheng and Du in [9, 16] from a three-phase approach: a matrix cell of ellipsoidal geometry surrounds each inclusion and in turn is surrounded by an unbounded medium with effective properties. In [26], the IDD model applied to conductive composites is presented.

By following this considerations, the localization tensors $\mathbb{A}_{\alpha}^{(\mathrm{IDD})}$ for the IDD model takes the form

$$\mathbb{A}_{\alpha}^{(\mathrm{IDD})} = \left(\boldsymbol{I} - \sum_{\beta=1}^{N} \mathsf{c}_{\beta} \left(\boldsymbol{k}_{\beta} - \boldsymbol{k}_{0} \right) \mathbb{A}_{\beta}^{(\mathrm{incl})} \mathbb{P}_{\beta}^{(\mathrm{cell})} \right)^{-1} \mathbb{A}_{\alpha}^{(\mathrm{incl})}, \tag{15}$$

where $\mathbb{P}_{\beta}^{(\mathrm{cell})}$ represents the Hill tensor of the β-th matrix cell.

To summarize, although MT scheme takes into account the inclusion interaction, it fails to account for the inclusion distribution and the interaction between inclusion and their immediate surrounding matrix material. On the other hand, PCW and IDD estimates do not present the aforementioned shortcomings and capture this information through the matrix cells. Figure 2 provides a graphic description of these schemes.

2.3. Relations between IDD, MT and PCW models

In order to study the connections between the mean-field approaches IDD, MT and PCW, a unified formulation should be considered, as proposed by [18], based on the links established earlier between these models in [16].

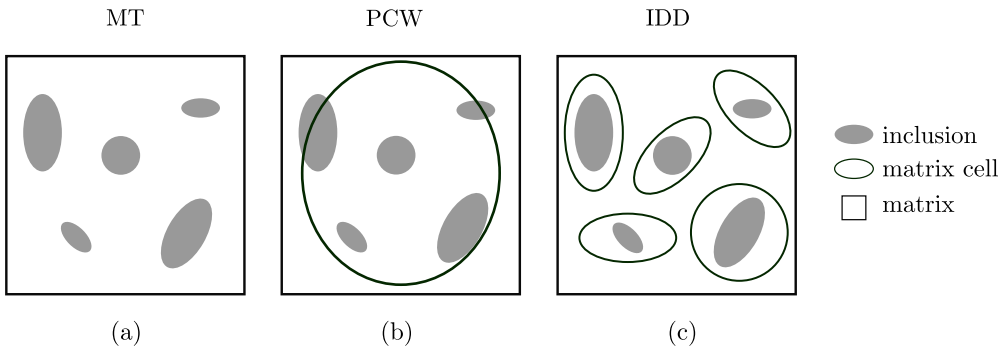

Figure 2: Diagrams of the mean-field models under study. (a) MT (no cell), (b) PCW (one general cell), (c) IDD (one cell per inclusion).

In this vein, after transformations on the localization tensor $\mathbb{A}_\alpha^{(\mathrm{MT})}$ of Eq. (13), the following result is obtained:

$$\mathbb{A}_\alpha^{(\mathrm{MT})} = \mathbb{A}_\alpha^{(\mathrm{incl})} \left(\boldsymbol{I} - \sum_{\beta=1}^{N} \mathsf{c}_\beta \mathbb{P}_\beta^{(\mathrm{incl})} (\boldsymbol{k}_\beta - \boldsymbol{k}_0) \mathbb{A}_\beta^{(\mathrm{incl})} \right)^{-1} . \tag{16}$$

Then, combining the three approximations, (14), (15) and (16) of mean localization tensors with the definition (11) of the effective conductivity, the three estimates are given in Table 1, with a transpose on the IDD estimate to stress the similarity of expressions. Indeed, the IDD estimate *may not be symmetric*, an important issue addressed in detail in Section 3.1 below.

Approaches	Effective conductivity tensors
MT	$\boldsymbol{k}_{\mathrm{eff}}^{(\mathrm{MT})} = \boldsymbol{k}_0 + \sum_{\alpha=1}^{N} \mathsf{c}_\alpha \left(\boldsymbol{k}_\alpha - \boldsymbol{k}_0\right) \mathbb{A}_\alpha^{(\mathrm{incl})} \left(\boldsymbol{I} - \sum_{\beta=1}^{N} \mathsf{c}_\beta \mathbb{P}_\beta^{(\mathrm{incl})} (\boldsymbol{k}_\beta - \boldsymbol{k}_0) \mathbb{A}_\beta^{(\mathrm{incl})} \right)^{-1}$,
PCW	$\boldsymbol{k}_{\mathrm{eff}}^{(\mathrm{PCW})} = \boldsymbol{k}_0 + \sum_{\alpha=1}^{N} \mathsf{c}_\alpha \left(\boldsymbol{k}_\alpha - \boldsymbol{k}_0\right) \mathbb{A}_\alpha^{(\mathrm{incl})} \left(\boldsymbol{I} - \mathbb{P}^{(\mathrm{cell})} \sum_{\beta=1}^{N} \mathsf{c}_\beta \left(\boldsymbol{k}_\beta - \boldsymbol{k}_0\right) \mathbb{A}_\beta^{(\mathrm{incl})} \right)^{-1}$,
IDD	${}^{\mathrm{T}}\boldsymbol{k}_{\mathrm{eff}}^{(\mathrm{IDD})} = \boldsymbol{k}_0 + \sum_{\alpha=1}^{N} \mathsf{c}_\alpha \left(\boldsymbol{k}_\alpha - \boldsymbol{k}_0\right) \mathbb{A}_\alpha^{(\mathrm{incl})} \left(\boldsymbol{I} - \sum_{\beta=1}^{N} \mathsf{c}_\beta \mathbb{P}_\beta^{(\mathrm{cell})} \left(\boldsymbol{k}_\beta - \boldsymbol{k}_0\right) \mathbb{A}_\beta^{(\mathrm{incl})} \right)^{-1}$.

Table 1: Unified formulation of the effective conductivity properties. The IDD estimate is transposed to stress the similarity of expressions.

As observed, the expressions in Table 1 are very similar, and when the IDD estimate

is symmetric, *i.e.* $\boldsymbol{k}_{\text{eff}}^{(\text{IDD})} = {}^{\text{T}}\boldsymbol{k}_{\text{eff}}^{(\text{IDD})}$, an interpretation of MT and PCW based on the IDD scheme can be provided, as discussed by [16, 18] and recalled now for completeness. In Figure 3 (a), the capability of IDD to account for inclusions and cells with different aspect ratios and orientations is illustrated. In contrast, the MT approach (see Figure 3 (b)) considers that inclusions and cells respectively share the same aspect ratio and orientation, which is achieved by setting $\mathbb{P}_\beta^{(\text{cell})} = \mathbb{P}_\beta^{(\text{incl})}$ in the IDD scheme (see Table 1). On the other hand, the PCW model behaves as if a common cell is chosen for all inclusions (see Figure 3 (c)), that is if all matrix cells have identical shape and orientation, which is obtained by similarly replacing $\mathbb{P}_\beta^{(\text{cell})} = \mathbb{P}^{(\text{cell})}$ in the IDD scheme (see Table 1).

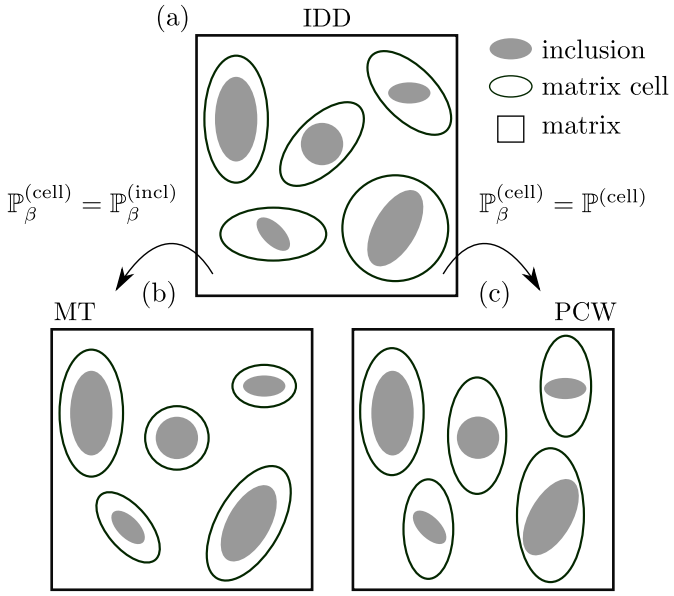

Figure 3: Diagrams of the unified formulation and the connections between the models.

Remark 1. *The double-inclusion approach proposed prior to IDD by [15] results in very similar estimates than IDD, and also embeds the MT and PCW models as special cases [27]. The question whether IDD and double-inclusion models are identical in all cases has not been answered yet, at the best of our knowledge, but is out of the scope of the present paper.*

In conclusion, IDD emerges as the most general approach among the studied models. It provides additional morphological criteria through the cells that take into account the spatial

distributions of inclusions and the interaction between inclusions and their immediately surrounding matrix. Such cell parameters should be chosen or derived from microstructural analyses. Some propositions are done by [28, 19], and a systematic approach is presented below.

3. Practical use of the IDD model

In this section, we address two key issues that have to be tackled to use effectively the IDD model, that is (i) how to account for its (possible) lack of symmetry and (ii) how to choose the matrix cells corresponding to each inclusion.

3.1. Addressing symmetry issues

In relation to the MT scheme, several studies have addressed the problem of loss of symmetry appearing in the effective tensor. For example, [29] dealt with two-phase composites and showed that if the composite is reinforced with isotropic inclusions of any morphology or with perfectly aligned fibers of any material symmetry, these are sufficient conditions to guarantee the symmetry of the MT tensor. Notice that the term "phase" stands for inclusions of assigned geometry and constituent material, regardless of orientation. In addition, the authors in [30] focused their study on multi-phase composites, and proved that the MT estimates is symmetric only for those multi-phase composites where all phases have similar shape and the same orientation.

On the other hand, the PCW estimation always satisfies the symmetry requirements for the effective tensor, see [14, 31].

Finally, regarding IDD, we proceed in a similar manner as was discussed in [18] and rewrite the IDD expression given in Table 1 as follows:

$$
\begin{aligned}
{}^{\mathrm{T}}\boldsymbol{k}_{\mathrm{eff}}^{(\mathrm{IDD})} &= \boldsymbol{k}_0 + \left(\left(\sum_{\alpha=1}^{N} \mathsf{c}_\alpha \left(\boldsymbol{k}_\alpha - \boldsymbol{k}_0 \right) \mathbb{A}_\alpha^{(\mathrm{incl})} \right)^{-1} - \mathbb{P}^{(\mathrm{IDD})} \right)^{-1} \\
\text{with:} \quad \mathbb{P}^{(\mathrm{IDD})} &= \sum_{\beta=1}^{N} \mathsf{c}_\beta \mathbb{P}_\beta^{(\mathrm{cell})} \left(\boldsymbol{k}_\beta - \boldsymbol{k}_0 \right) \mathbb{A}_\beta^{(\mathrm{incl})} \left(\sum_{\alpha=1}^{N} \mathsf{c}_\alpha \left(\boldsymbol{k}_\alpha - \boldsymbol{k}_0 \right) \mathbb{A}_\alpha^{(\mathrm{incl})} \right)^{-1}, \qquad (17)
\end{aligned}
$$

Note that this is almost exactly the PCW expression (see Table 1), only with $\mathbb{P}^{(\text{cell})}$ replaced by $\mathbb{P}^{(\text{IDD})}$. The symmetry of the IDD model is thus guaranteed when this tensor $\mathbb{P}^{(\text{IDD})}$ is symmetric, since $(\boldsymbol{k}_\alpha - \boldsymbol{k}_0)\,\mathbb{A}_\alpha^{(\text{incl})}$ is always symmetric. This is in particular the case in the following configurations:

1. the MT model is used (Figure 3(b)) and one of the sufficient conditions given above for the symmetry of the MT estimate is satisfied;
2. the PCW model is used (Figure 3(c));
3. all inclusions are identical except for their size, *i.e.* have same aspect ratios, orientation and constitutive material, and therefore localization tensors: $\mathbb{A}_\alpha^{(\text{incl})} = \mathbb{A}^{(\text{incl})}$. In this case, one obtains
$$\mathbb{P}^{(\text{IDD})} = \frac{1}{\mathsf{c}_\text{I}} \sum_{\beta=1}^{N} \mathsf{c}_\beta \mathbb{P}_\beta^{(\text{cell})}, \qquad \text{with } \mathsf{c}_\text{I} = \sum_{\alpha=1}^{N} \mathsf{c}_\alpha \tag{18}$$
which is symmetric as a sum of symmetric Hill's tensors;
4. all inclusions are circular (in 2D) or spherical (in 3D) and made of isotropic but not necessarily identical materials, with conductivity tensors $\boldsymbol{k}_\alpha = k_\alpha \boldsymbol{I}$. In this case, the localization tensors are isotropic (proportional to identity) and the expression (17) of $\mathbb{P}^{(\text{IDD})}$ again becomes a weighted sum of symmetric Hill tensors. In 2D, with the expressions given in Appendix B.2 one obtains:
$$\mathbb{P}^{(\text{IDD})} = \sum_{\beta=1}^{N} \mathsf{c}_\beta \mathbb{P}_\beta^{(\text{cell})} \frac{2(k_\beta - k_0)}{\gamma_\beta + 1} \left(\sum_{\alpha=1}^{N} \mathsf{c}_\alpha \frac{2(k_\alpha - k_0)}{\gamma_\alpha + 1} \right)^{-1} \qquad \text{(2D case)} \tag{19}$$
where $\gamma_\alpha = k_\alpha / k_0$ are the conductivity contrasts. This last case is of interest when studying the behavior of composites reinforced with two (or more) kinds of long, unidirectional fibers by reducing the analysis in the (2D) transverse plane e.g. [20, Sect. 5.2.5]; or 3D composites containing both seemingly-spherical reinforcements and voids.

The third and fourth cases above are configurations where IDD can be used "as it is", without reducing to one of the two other models. The third one will be used in the ensuing numerical examples for comparisons. To address the cases where symmetry is not guaranteed, while still accounting for the relevant information given by the individual cells, we now propose two methods.

3.1.1. Calibrating the PCW model using individual cells

The first natural idea that comes to mind is to use the PCW model, which is always symmetric. The question then is the choice of the distributional cell and the corresponding tensor $\mathbb{P}^{(\mathrm{cell})}$. Based on the third case and on expression (18) just above, we propose the following choice for this tensor:

$$\mathbb{P}^{(\mathrm{cell})} := \frac{1}{\mathsf{c}_\mathrm{I}} \sum_{\alpha=1}^{N} \mathsf{c}_\alpha \mathbb{P}_\alpha^{(\mathrm{cell})}. \tag{20}$$

In this way, IDD and PCW models coincide in cases 2 and 3 discussed above (identical cells and identical inclusions), and the IDD-inspired PCW symmetric estimate whose distributional tensor is given by (20) can be used in other configurations. This distributional tensor is used for the numerical simulations of the PCW model in Section 5 below.

3.1.2. Two-step homogenization process

Another approach for dealing with the symmetry issue of the MT model was proposed in [20] and followed by many afterwards, *e.g.* [32]. A two-step homogenization scheme is applied to compute the effective properties combining MT and the upper and lower bounds of Voigt and Reuss, respectively, namely

$$\boldsymbol{k}_{\mathrm{eff}}^{(\mathrm{Voigt})} := \sum_{\alpha=0}^{N} \mathsf{c}_\alpha \boldsymbol{k}_\alpha, \tag{21a}$$

$$\boldsymbol{k}_{\mathrm{eff}}^{(\mathrm{Reuss})} := \left(\sum_{\alpha=0}^{N} \mathsf{c}_\alpha (\boldsymbol{k}_\alpha)^{-1} \right)^{-1}. \tag{21b}$$

Here, instead of using MT, we adopt the IDD scheme for the first homogenization step. Figure 4 describes the two-step homogenization process. The domain is first decomposed into as many regions as there are families of identical inclusions. These regions behave as a two-phase material where the volume fraction of inclusions in each grain is the same as the total volume fraction of inclusions in the original composite. As a result, the symmetry of the IDD tensor is guaranteed in all the regions, as discussed in Section 3.1 above. Then, in the first homogenization step we apply the IDD scheme, obtaining the effective properties of

each grain individually. The last step is to homogenize over all the grains by means of Voigt and Reuss bounds. We will refer this approach as IDD-Voigt and IDD-Reuss, respectively.

Remark 2. *Other approaches could be used for the second step, as long as they preserve the symmetry of the estimate,* e.g. *another PCW model (but with another distributional cell to be determined), or a self-consistent model. Considering that the geometric features of the microstructure are accounted for by the IDD step, we chose the Voigt and Reuss estimates for the second one for simplicity.*

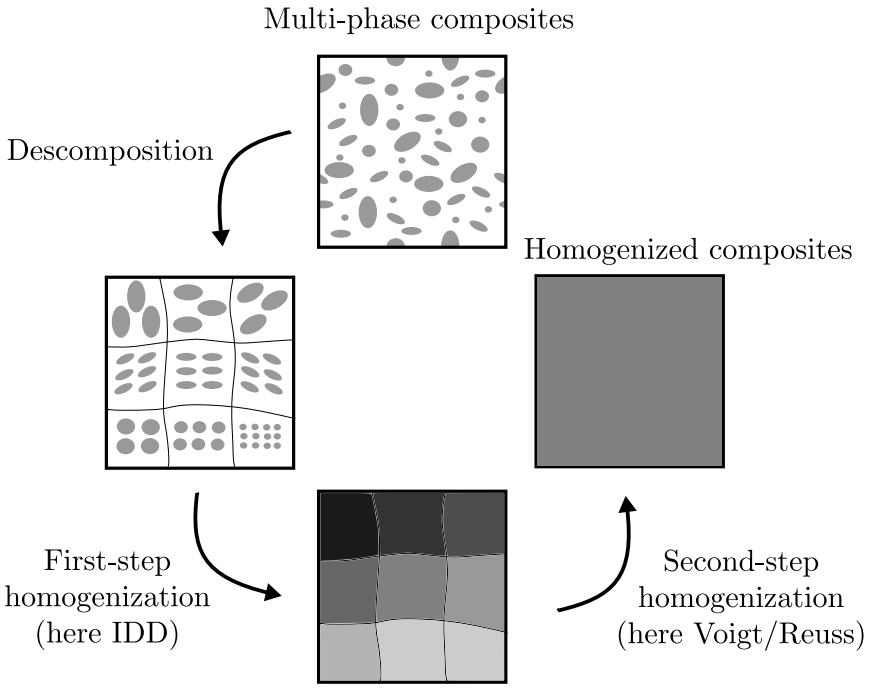

Figure 4: Two-step homogenization procedure.

3.2. Cells selection via inertia equivalence and Voronoï diagrams

Until now, a comprehensive discussion of the IDD scheme has been provided. However, beyond the particular case where IDD is reduced to MT (see Figure 3), the lack of clarity on how to select the matrix cells (or cell, for the PCW model) still persists. In this regard, we propose a methodology to derive the required information of the cells from a microstructural

analysis of a representative image. This data will serve not only as input for IDD, but also for applying the PCW scheme as proposed in Section 3.1.1 above. The approach represents one of the main novelties of the present work.

More precisely, we look at the practical implementation of the *inertia equivalence* procedure proposed by [16] (see Figure 5) but applied only for inclusions distributed on periodic lattices [17], to the best of our knowledge. The idea is to consider regular polyhedrons (polygons in 2D) to partition the matrix domain such that each of these subdomains or cells are made up of an inclusion as a nucleus and an immediate surrounding matrix material region as the atmosphere. Then, since non-ellipsoidal cells are obtained to assemble the space, the procedure follows by assigning a matching ellipsoid to each polyhedral cell. In the procedure, the polyhedron is further substituted by an equivalent ellipsoid that has the same moment of inertia as the region. For instance, if the tessellation polygons are rectangles (e.g. in the case of a bi-periodic distribution of inclusions), then elliptical cells are proportional to the maximal inscribed ellipses.

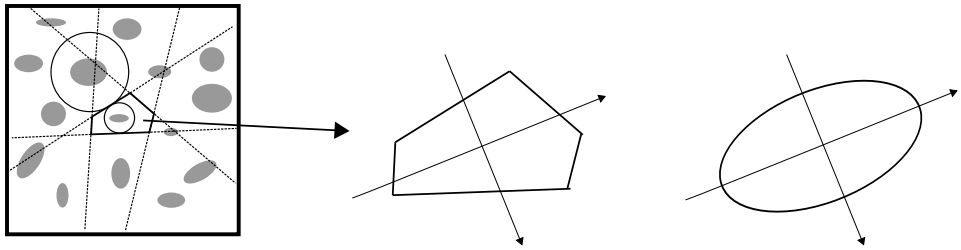

Figure 5: Inertial equivalence in 2D. a) Partition in polygonal cells. b) A polygonal cell. c) Equivalent elliptical cell with the same geometrical moment. This figure is inspired by Figure 4 of [16].

To determine these polyhedral cells, we quote [16] (with our notation): *"For any given inclusion $\mathscr{V}_\alpha$, to define the inclusion-matrix cell $\mathscr{V}_\alpha^{(\text{cell})}$ we can introduce a plane between $\mathscr{V}_\alpha$ and its any neighboring inclusion $\mathscr{V}_\beta$ that is perpendicular to the line linking the centers of $\mathscr{V}_\alpha$ and $\mathscr{V}_\beta$ and partitions this line in accordance with the ratio of the radii of $\mathscr{V}_\alpha$ and $\mathscr{V}_\beta$"*. This description naturally relates to Voronoï diagrams [33, 34, 35].

The Voronoï diagram of a given set of discrete points in a Euclidean space, also called "seeds", is a partition of the space into regions, which contain the points of the space closer

to a given seed than to any other. Let $\mathbf{X}$ be a metric space with distance function d, then, the Voronoï cell $\mathscr{R}_k$, associated with the seed P_k is defined as follows,

$$\mathscr{R}_k = \{\, x \in \mathbf{X} \mid d(x, P_k) \leq d(x, P_j) \text{ for all } j \neq k\}. \tag{22}$$

A natural extension to a *multiplicatively weighted* Voronoï diagram is given by the following definition of a cell:

$$\mathscr{R}_k = \{\, x \in \mathbf{X} \mid d(x, P_k) \,/\, r_k \leq d(x, P_j) \,/\, r_j \text{ for all } j \neq k\}, \tag{23}$$

where r_k and r_j are the weights associated with the seeds P_k and P_j, respectively.

The definition of the multiplicatively weighted Voronoï diagram has a strong analogy with the aforementioned approach given in [16], with the Voronoï weights determined by the inclusions radii. However, as a drawback of using this tessellation, Voronoï cells in a multiplicative scheme exhibit circular arcs instead of straight lines, may be disconnected and have holes. We refer to [36] for a detailed study of the multiplicative case with applications in two-dimensional cellular tissues.

Based on the above considerations, in this paper we propose to use the classical Voronoï diagram as the tessellation method, and thus obtain the polygonal cells that will then be replaced by the equivalent ellipses with the same moment of inertia as the region. Although the classical Voronoï diagram does not seem to conform completely to the authors' original idea, it might be worth to explore it as a first approximation. Its performances and drawbacks will be discussed in Section 6.

4. Methods, modeling and numerical tools

The aim of this section is to discuss the main set of tools and methods that have been used to produce the numerical comparisons presented in the next section. These tools were implemented in an home-made Python library "PyHom: a Python library for homogenization" whose main functions are represented in Figure 6.

This computational and homogenization-based approach is conceived for calculating the effective conductivity properties of composite materials with complex micro-structures in a

2D framework. The backbone of the library relies on the theory described above, and uses not only existing image processing modules, but also functionality and packages built by the authors. The main interest is using PyHom as a toolbox to study the core issues in the application of IDD and PCW, and to understand in essence how these mean-field methods work.

Hereafter, we describe in more detail the choices we made for the key step of the process, namely (i) RVE generation, (ii) image analysis and Voronoï diagram generation and (iii) homogenized estimates computation.

4.1. Generating representative elements

To ease the comparisons between models, we generate artificial RVE with controlled distributions of inclusions. The two sections below present the methods chosen to generate these RVE.

4.1.1. RSA algorithm to place elliptic inclusions with prescribed distribution

We start by specifying the Random Sequential Adsorption (RSA) algorithm [33] more closely and see how it can be applied to build a heterogeneous microstructure in a 2D framework. Let us first recall that in the RSA algorithm, the position of a test particle is generated following a uniform distribution. If the test particle intersects with any of the previously added particles, it is discarded; otherwise, the test particle is added to the collection.

Table 2 and Figure 7 present an example of RVE construction. A number $N^{(\text{incl})}$ of elliptical inclusions, whose aspect ratio $e^{(\text{incl})}$ and orientation $\theta^{(\text{incl})}$ are specified, should be placed to reach a volume fraction $c^{(\text{incl})}$ (which determines the size of these inclusions). To obtain a controlled distribution not only due to the inclusion shape, elliptical *exclusion zones*, which we refer to as RSA cells, are placed first. Aspect ratio $e^{(\text{cell-RSA})}$ and orientation $\theta^{(\text{cell-RSA})}$ of these cells are also specified *a priori*, as well as a security factor to prevent contact between cells, see Figure 7(a). Their size is determined from a size factor that is the ratio between inclusion and cells major axis.

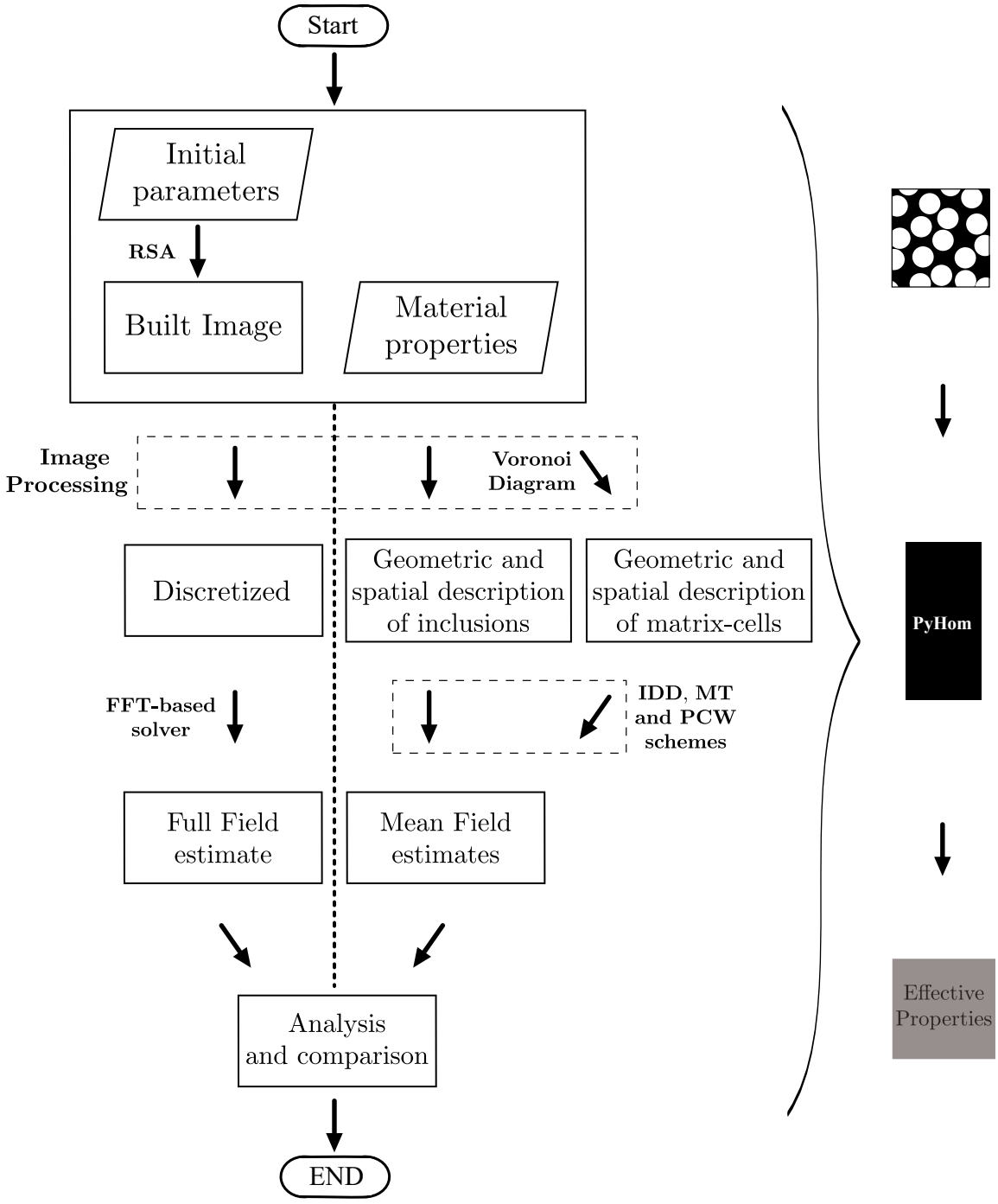

Figure 6: Workflow sketch for the numerical comparison of homogenized estimates for various microstructures.

pixels	$N^{(\text{incl})}$	$c^{(\text{incl})}$	$e^{(\text{incl})}$	$\theta^{(\text{incl})}$	$e^{(\text{cell-RSA})}$	$\theta^{(\text{cell-RSA})}$	security factor	size factor
256	8	0.05	0.5	-$\pi/4$	0.7	$\pi/4$	1.3	0.5

Table 2: Parameters for the example RVE represented in Figure 7.

As seen on Figure 7(b), the resulting RVE is periodized to facilitate the full-fields computations, *i.e.* inclusions that cross the edges are duplicated. This also ensures that the chosen volume fraction is reached within the RVE, up to discretization. Finally, an image is generated with a prescribed discretization (256×256 pixels in all the upcoming examples), see Figure 7(c). This image will be the input of both full-fields and image-based mean-fields homogenization methods, as indicated in Figure 6.

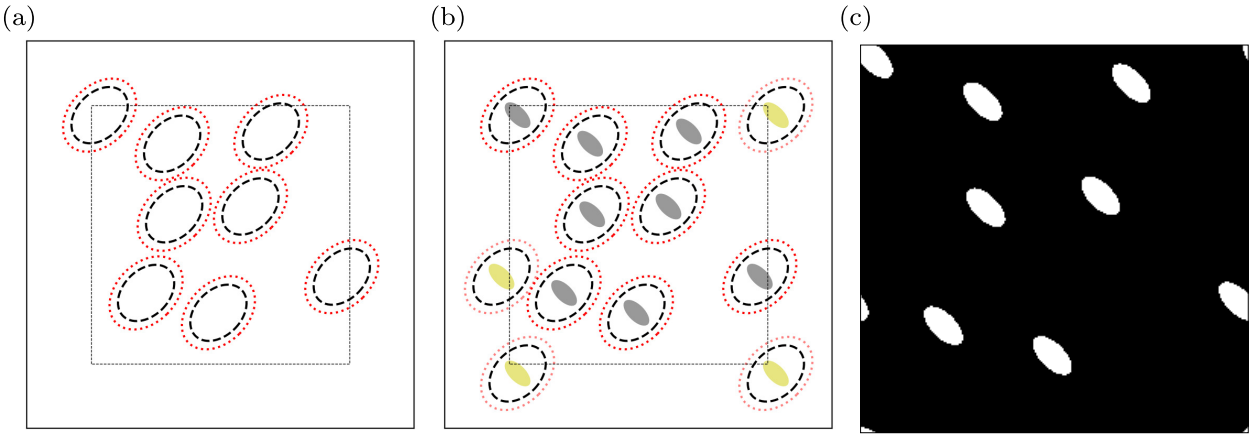

Figure 7: Example of RVE construction using an RSA algorithm. (a) Placement of eight RSA cells: dashed and dotted lines design the cells and their amplification by the security factor, respectively. (b) Placement of inclusions in the central points of the RSA cells and duplication of the inclusions that cross the edges. (c) Final image of the microstructure.

4.1.2. Advani-Tucker law for orientation distributions

To generate distribution of non-aligned inclusions, we use the Advani-Tucker law for orientation distributions. In [37], this distribution function is proposed to describe an aligned and axisymmetric orientation state in a 3D configuration, see for instance [37, 19, 38]. The explicit form of the distribution function, adapted for a 2D microstructure, is rewritten as

follows,

$$f(\theta) = K \sin^{m_{\mathrm{AT}}}(\theta), \tag{24}$$

where K is a normalization constant and, $\theta \in [0, \pi]$ is the inclusion orientation with respect to the chosen privileged direction.

This law is characterized by a single parameter m_{AT}. Two extreme cases arise when $m_{\mathrm{AT}} = 0$ for which the law reduces to the uniform distribution, and when $m_{\mathrm{AT}} \to \infty$, for which aligned inclusions are recovered.

4.2. Derivation and analysis of Voronoï diagram with Python libraries

To build and exploit the Voronoï diagrams needed for distribution analysis, as proposed in Section 3.2, we use two Python libraries: *scikit.image* [39] for image analysis, and *scipy* [40] for Voronoï diagram generation.

Figure 8 presents the process applied to the example image presented in Figure 7. First, *scikit.image* [39] is used to partition the image between subdomains (matrix and inclusions), to extract the characteristics of the inclusions (number, size, aspect ratio, orientation) and to position their centers, see Figure 8(a). Then, these centers are cloned on a 3×3 grid, see Figure 8(b), and the Voronoï diagram is generated by *scipy*. The regions of interest of this Voronoï diagram will consist of the colored closed polygons, while the outermost regions of the diagram (including unbounded cells) are not involved in the analysis. This generated diagram is then isolated, see Figure 8(c).

To analyze this diagram, the same image processing tool can be used: again the library *scikit.image* [39] is used to partition the image Figure 8(c) into distinct cells, whose properties are extracted (function *regionprops* in modulus *mesure*). These properties notably include the lengths of the minor and major axis of the ellipse with the same moment of inertia as the region, as required by the proposal of Section 3.2. Figure 9 finally shows the elliptic cells resulting from this analysis, along with the inclusions determined in the first step.

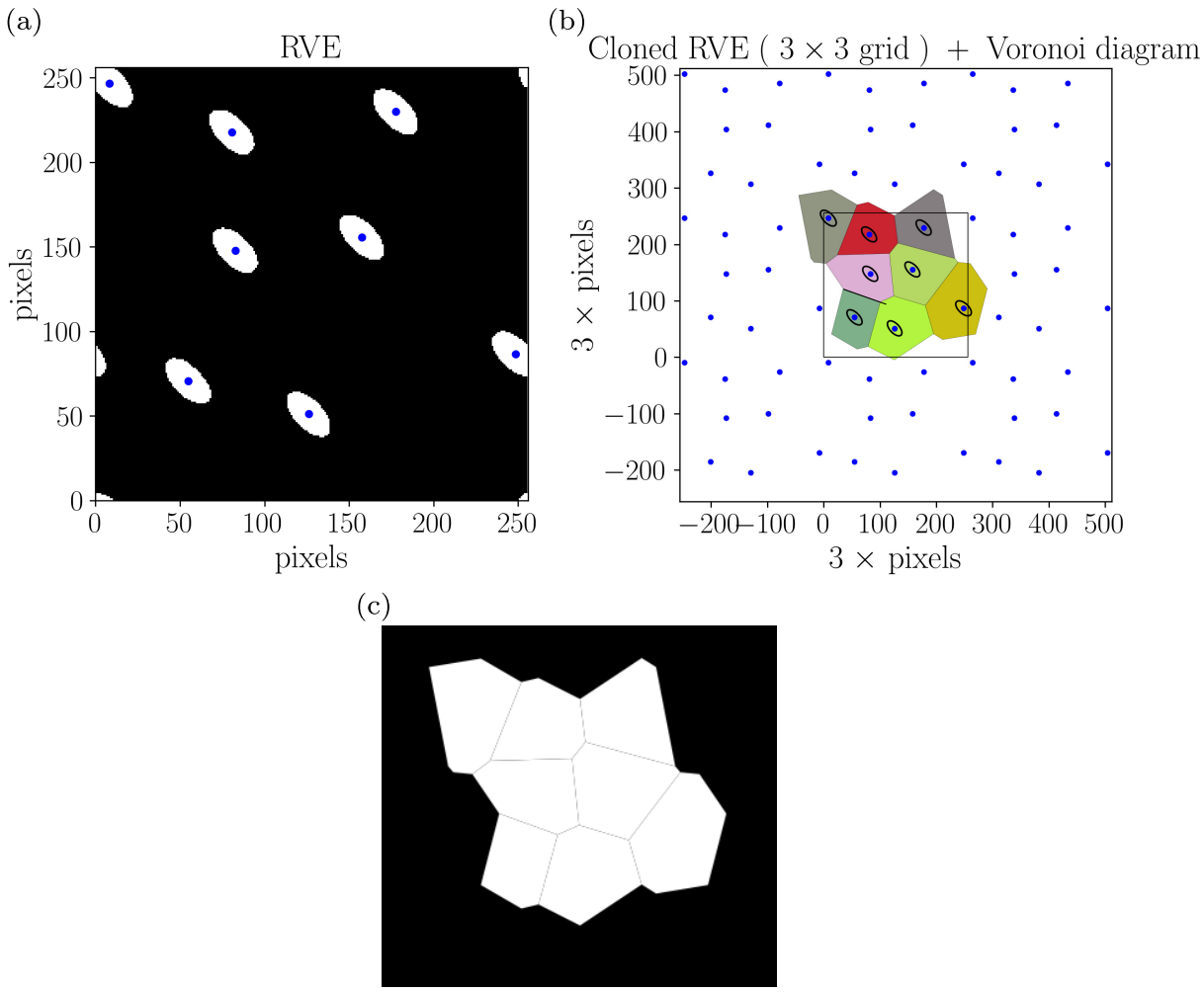

Figure 8: Voronoï diagram built from image analysis (image built in Figure 7) (a) Center of inclusions. (b) Cloned RVE. (c) Derived Voronoï diagram.

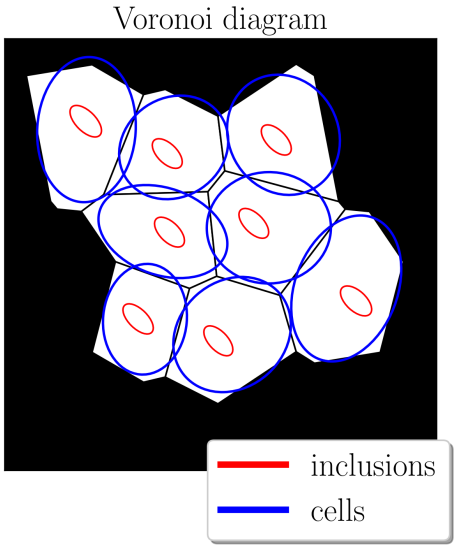

Figure 9: Final result of image analysis: inclusions and elliptic cells determined from the Voronoï diagram.

4.3. FFT-based solver

Reference effective properties are computed using the full-field approach described in Section Appendix A. To solve the elementary problem, a FFT-based solver was implemented in Python. In this work addressing only 2D linear conductivity with moderate material contrasts, the "basic scheme" proposed in the seminal papers of Moulinec and Suquet [41, 42] was chosen for its simplicity of implementation, although many improved FFT-based solvers have been developed in the last decade, see *e.g.* [5, 6].

5. Numerical results and comparisons

In this section, we analyze different microstructures, and proceed to compute and compare their effective conductivity properties. For the sake of simplicity and focus on spatial distribution, the heterogeneous material $\mathscr{B}$ is assumed to be constituted by a matrix reinforced by elliptical inclusions with different aspect ratios and orientations, both the matrix and inclusions being isotropic phases.

The results are presented in terms of the principal components of the conductivity tensors (*i.e.* their eigenvalues), denoted $k_{\text{eff-I}}$ and $k_{\text{eff-II}}$, with the convention $k_{\text{eff-I}} \geq k_{\text{eff-II}}$, correspond-

ing to the conductivities in the main directions (*i.e.* normalised eigenvectors) $\mathfrak{n}_1$ and $\mathfrak{n}_2$. The angle $\theta_{\text{eff}} := (\mathfrak{e}_1, \mathfrak{n}_1)$, called the *orientation of the conductivity tensor* afterwards, is used to specify these main directions. The notations are represented in Figure 10, where notations for main axes $\mathfrak{a}_1$ and $\mathfrak{a}_2$, and orientation $\theta^{(\text{incl})}$ of inclusions are also depicted.

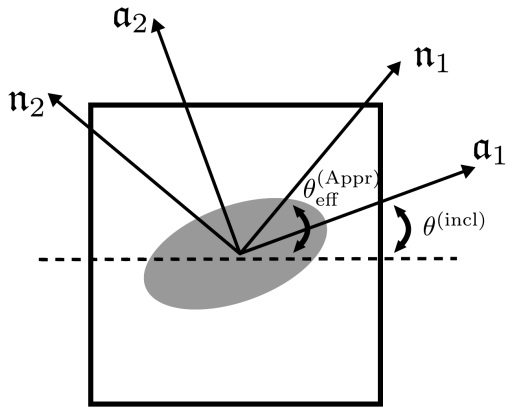

Figure 10: Notations for the orientations of inclusions and effective conductivity tensor.

Moreover, the *normalized* properties (by the matrix' conductivity k_0) are given. See Appendix B.1 for simplified formula of effective estimates in this case, and Appendix B.2 for more details about the expressions of the localization and Hill tensors involved in the calculations, $\mathbb{A}_\alpha^{(\text{incl})}$ and $\mathbb{P}_\alpha^{(\text{cell})}$, respectively.

5.1. Case 1: Anisotropic distribution, identical inclusions

The first case of interest concerns identical isotropic inclusions distributed in an anisotropic way in an isotropic matrix. In particular, for *circular* inclusions, the expected anisotropy of effective conductivity is due to this distribution only. To do so, we generate the microstructure using elliptic RSA-cells by following the process described in Section 4.1.1. The parameters given in Table 3, in the case of circular inclusions, are utilized and result in RVE as the one plotted in Figure 11.

Before going further, the statistical representativity of this RVE is verified by computing the effective properties of 10 different RVE generated this way. The results, plotted in appendix in Figure C.24, show that the difference between the properties of each of these

pixels	$N^{(\text{incl})}$	$c^{(\text{incl})}$	$e^{(\text{incl})}$	$\theta^{(\text{incl})}$	$e^{(\text{cell-RSA})}$	$\theta^{(\text{cell-RSA})}$	security factor	size factor
256	30	0.15	1	0	0.5	0	1.02	0.375

Table 3: Elliptic RSA cells and identical inclusions (circular here): chosen parameters for RVE generation, as represented in Figure 11.

RVE and their mean over the entire collection is less than 0.5%, and an individual RVE is therefore considered representative of the chosen microstructure.

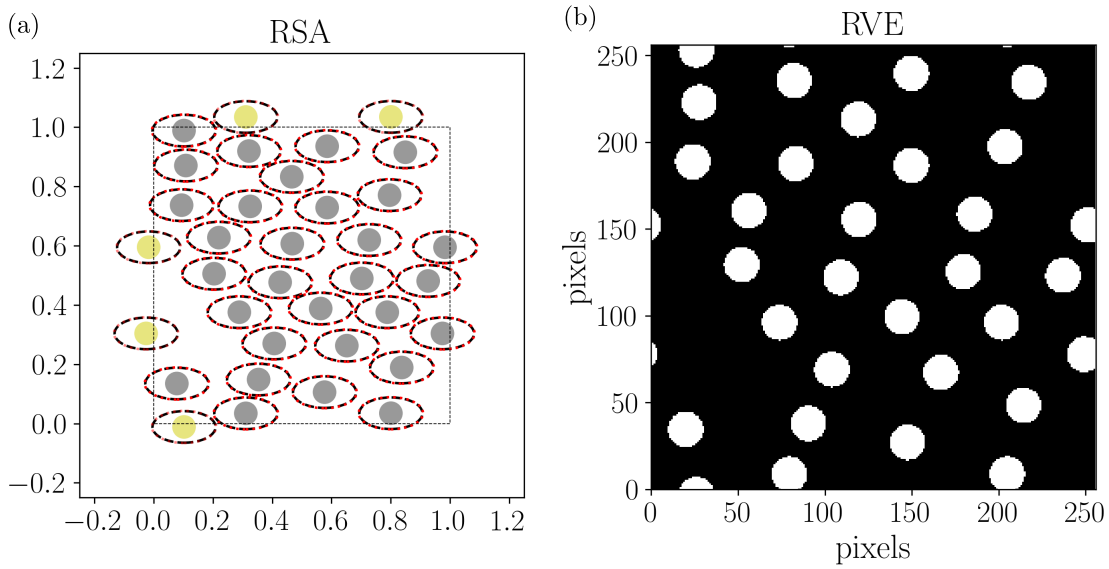

Figure 11: Elliptic RSA cells and identical inclusions (circular here): (a) RSA process (see Section 4.1.1) with the parameters of Table 3. (b) RVE of the 2D microstructure.

Now, the study is focused on a single microstructure, specifically the one shown in Figure 11. In this regard, Figure 12 (a) shows the corresponding Voronoï diagram in the background, along with the circular inclusions and inertially equivalent elliptical cells, highlighted in red and blue color, respectively. Notice that the Voronoï diagram has resulted in elliptical cells with several shapes and orientations, therefore, in the particular case of IDD model, we must consider as many Hill tensors as available cells (see Eq. (B.1c)).

In addition, Figure 12 (b) shows the scatter plot between aspect ratios e and orientations θ corresponding to the inclusions and cells, using dots and the previously assigned color. We

also display the mean value of the properties of the cells by means of a black star, and the pair $(\theta^{(\text{cell-PCW})}, e^{(\text{cell-PCW})})$ corresponding to the orientation and aspect ratio of the global cell using in the PCW scheme, obtained from the definition proposed in Eq. (20), and indicated on the graph with a purple square.

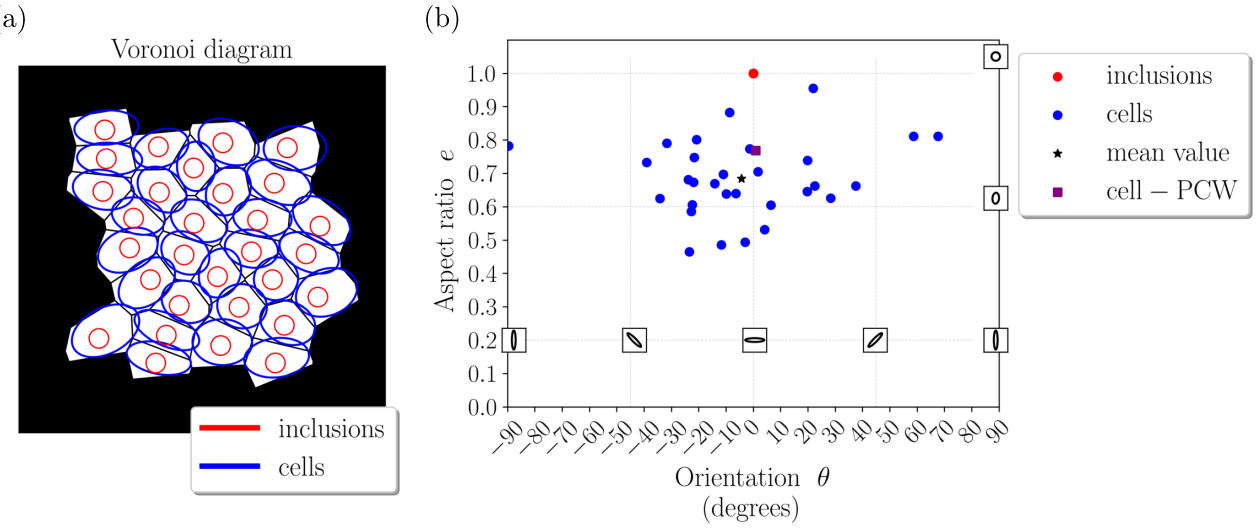

Figure 12: Elliptic RSA cells and identical inclusions (circular here): (a) Voronoï diagram, inclusions and respective cells. (b) Scatter plot between aspect ratio and orientation.

Since we utilize the classical Voronoï diagram as outlined in Subsection 3.2, the only parameters that influence its construction are the count and spatial arrangement of the inclusions. This means we can use the same Voronoï diagram to perform computations on microstructures that vary in geometrical features such as volume fraction, aspect ratio, or orientation of the inclusions, and also, in the conductivity contrast.

Following this idea, Figure 13 shows the normalized effective conductivity properties for the microstructure of Figure 11 (b), but varying the aspect ratio $e^{(\text{incl})}$ and orientation $\theta^{(\text{incl})}$ of the inclusions, and the conductivity contrast γ. The comparisons are made between MT, IDD and the FF numerical approach: in this case IDD and PCW models coincide using the definition of Eq. (20) for the PCW "distribution" tensor.

In Figure 13 (a) we highlight two situations relevant to the analysis. The first one, denoted by (I), corresponds to the value $e^{(\text{incl})} = 0.6$ and $\theta^{(\text{incl})} = 0°$, where the MT scheme offers

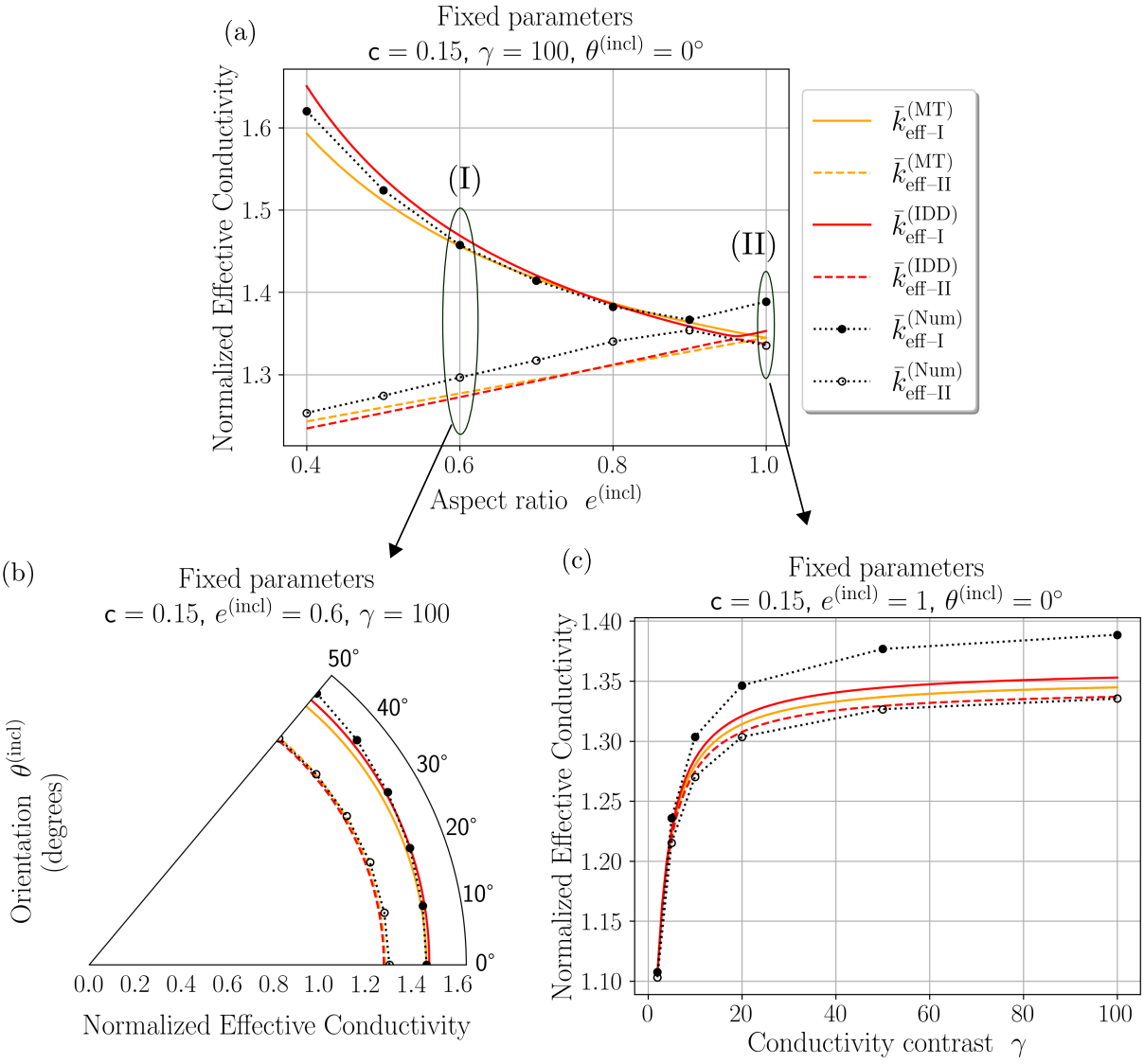

Figure 13: Elliptic RSA cells and identical inclusions: performance of MT and IDD models in comparison with the FF reference results. (a) Fixed orientation and conductivity contrast, varying aspect ratio of inclusions. (b) Fixed elliptic shape and conductivity contrast and varying orientations. (c) Fixed circular shape, varying conductivity contrast. In all case, the volume fraction of inclusions is 15%.

better results than IDD in comparison to the FF numerical approach. Nevertheless, in Figure 13 (b) it is observed that by varying the orientation and fixing the remaining parameters, IDD arises with better agreements. The second one (II) refers to the phenomenon of "geometrical" anisotropy that we mentioned at the beginning of the Section for circular inclusions.

For these circular inclusions, the MT scheme could not capture a possible geometrical anisotropy coming from the distribution of inclusions. In contrast, IDD does identify such anisotropy. The results are shown in Figure 13 (c) for different conductivity contrast γ. While quantitative accuracy is missing as both models underestimate $k_{\text{eff-I}}$, this qualitative improvement is a major advantage of the IDD model. This capability of capturing some of the anisotropy resulting from the distribution is also illustrated in Figure 14 for elliptic inclusions. The orientation of the MT effective tensor is again entirely given by the orientation of inclusions while the IDD model captures a small amount of the orientation difference observed on FF results due to the distribution.

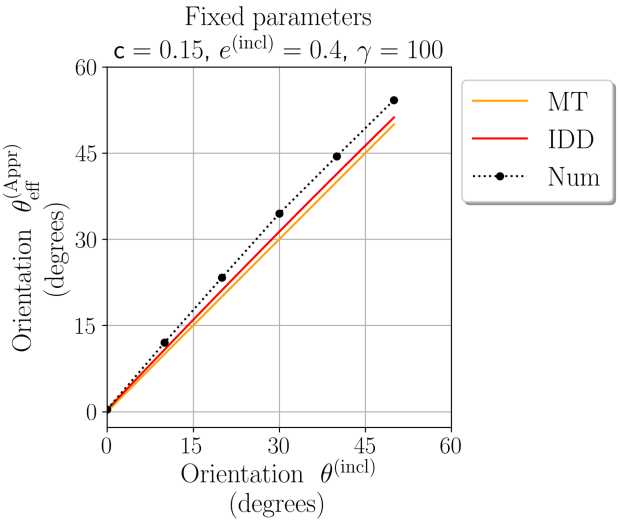

Figure 14: Elliptic RSA cells and identical elliptic inclusions: directions of anisotropy of the effective tensors, as a function of orientations of inclusions.

5.2. Case 2: Approximately isotropic distribution and aligned elliptic inclusions

In contrast to Section 5.1, here, we aim to arrange identical elliptical isotropic inclusions in an approximately isotropic way within an isotropic matrix, so that the anisotropy comes

mainly from the orientation and aspect ratio of the elliptical inclusions. For this purpose, we consider circular RSA-cells and the set of parameters shown in Table 4. Figure 15 illustrates a possible RVE that can be constructed under these considerations.

pixels	$N^{(\text{incl})}$	$c^{(\text{incl})}$	$e^{(\text{incl})}$	$\theta^{(\text{incl})}$	$e^{(\text{cell-RSA})}$	$\theta^{(\text{cell-RSA})}$	security factor	size factor
256	30	0.2	0.4	0	1	$\theta^{(\text{incl})}$	1.02	1

Table 4: Circular RSA cells and elliptic inclusions : chosen parameters for RVE generation, as represented in Figure 15.

Again, we verified that the chosen RVE is statistically representative by comparing the properties of 10 RVE generated with the same parameters, see Figure C.25 in appendix. The maximum difference of the larger conductivity $k_{\text{eff-I}}$ with its mean value over the collection of RVE is this time larger, about 2.5%, but we still consider an individual RVE as representative.

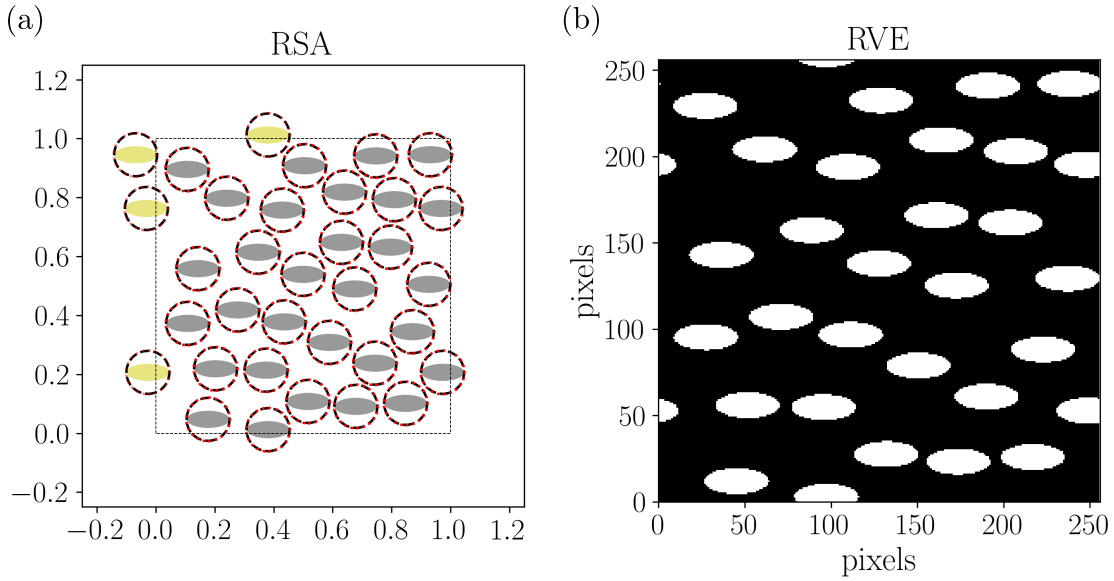

Figure 15: Circular RSA cells and elliptic inclusions: (a) RSA process. (b) 2D representative element of the microstructure.

Figure 16 (a) shows the Voronoï diagram corresponding to the microstructure of Figure 15 (b), along with the elliptical inclusions and the different inertially equivalent elliptical cells. Moreover, in Figure 16 (b) we present the scatter plot between aspect ratios e and

orientations θ corresponding to the inclusions, cells, the mean value of the cell properties, and the pair $(\theta^{(\text{cell-PCW})}, e^{(\text{cell-PCW})})$. In contrast to what was observed in Figure 12 (b), while the cells remain elliptical, their aspect ratios approach unity and the orientations exhibit a greater dispersion across the range of values. This is an expected result from the choice of circular RSA-cells to generate the microstructure.

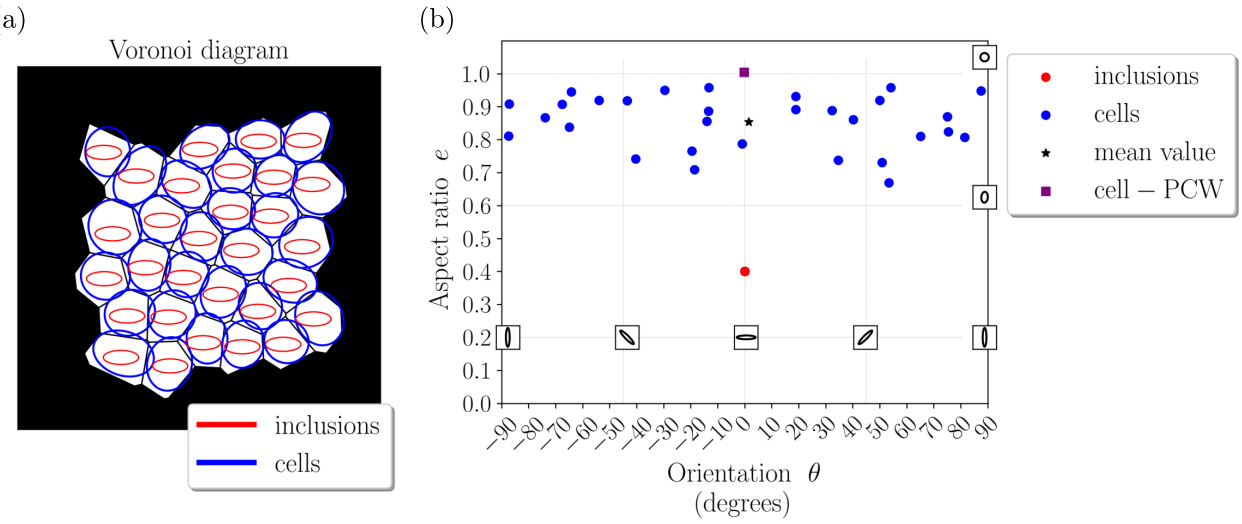

Figure 16: Circular RSA cells and elliptic inclusions: (a) Voronoï diagram, inclusions and respective cells. (b) Scatter plot between aspect ratio and orientation.

The normalized effective conductivity properties of the microstructures obtained by varying the aspect ratio $e^{(\text{incl})}$ and orientation $\theta^{(\text{incl})}$ of the inclusions are given in Figure 17. Again, for identical inclusions the IDD and PCW models coincide. As observed in Figure 17 (a), the IDD scheme has a better agreement than MT with the FF numerical approach. Furthermore, in Figure 17 (b) we set the value of the largest discrepancy between MT and IDD, *i.e.* , $e^{(\text{incl})} = 0.4$, and study the behavior of the properties when varying the orientation of inclusions. The results are still favorable for IDD, proving in this case a clear quantitative gain compared to MT.

For completeness, we show in Figure 18 the comparison between the orientations of effective tensors for the different schemes, which are clearly given by the orientations of inclusions, as expected for this nearly-isotropic distribution.

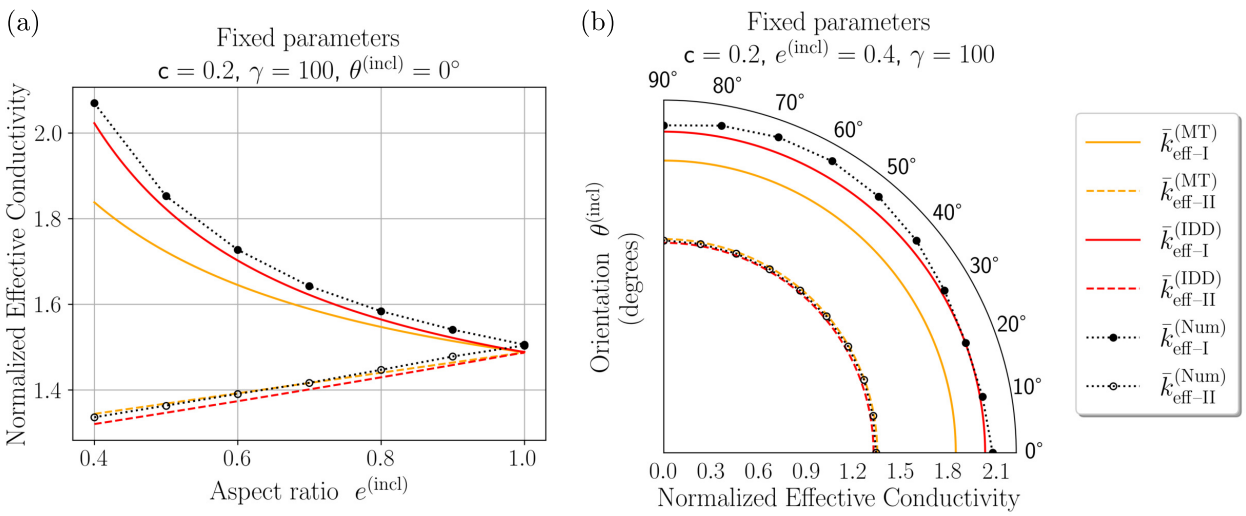

Figure 17: Circular RSA cells and elliptic inclusions: MT and IDD performance compared to the FF numerical approach for different aspect ratios and orientations of inclusions.

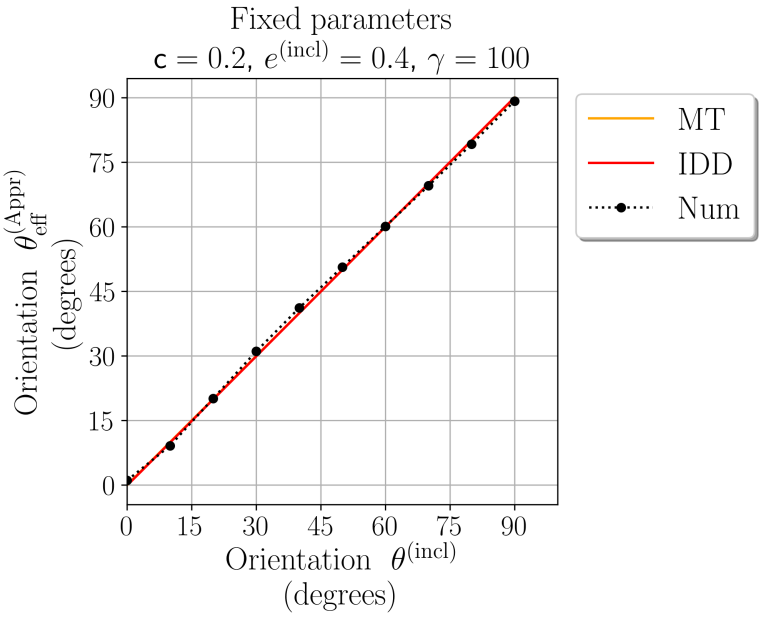

Figure 18: Comparison between the directions of anisotropy.

5.3. Case 3: Non-aligned inclusions

In this section, we proceed to investigate a scenario in which the inclusions are not aligned, *i.e.* cases where the effective conductivity tensor of the IDD model loses its symmetry. To this end, we consider microstructures in which all inclusions are identical except for their orientation. Two examples are considered: (i) manually chosen orientations and (ii) orientations following the Advani-Tucker law. In both cases, the RSA-cells are chosen identical to each inclusion (slightly magnified by a security factor), and the distribution is therefore only constrained by the inclusion shapes, contrarily to the previous cases.

5.3.1. Inclusion orientation chosen in a given set

For this part, the parameters utilized in the RSA algorithm are presented in Table 5, where θ_{sample} is a set of 30 orientation values manually selected from the set of values $\{-60, -45, -30, 0, 10, 25, 50, 75\}$ degrees. Figure 19 presents the obtained RVE.

pixels	$N^{(\text{incl})}$	$c^{(\text{incl})}$	$e^{(\text{incl})}$	$\theta^{(\text{incl})}$	$e^{(\text{cell-RSA})}$	$\theta^{(\text{cell-RSA})}$	security factor	size factor
256	30	0.2	0.5	θ_{sample}	$e^{(\text{incl})}$	$\theta^{(\text{incl})}$	1.1	1

Table 5: Elliptic inclusions with different orientations: chosen parameters for RVE generation, as represented in Figure 19.

Then, Figure 20 (a) presents the Voronoï diagram corresponding to the inclusions and the inertia-equivalent cells. Figure 20 (b) displays the aspect ratios and orientations for both the inclusions and cells, as well as the mean values for the cell properties and the corresponding values obtained using the PCW method. It can be observed that the orientations of the inclusions are grouped into eight families of values, as previously mentioned in the microstructure construction details.

Due to the loss of symmetry in the effective tensor computed with the IDD method, we apply the approach outlined in Section 3.1.2 and display in Figure 21 the normalized effective conductivity properties obtained with the two-step approaches (IDD-Voigt and IDD-Reuss) and the IDD-inspired-PCW model. The three approaches yield similar results, the PCW estimates being somewhat in-between IDD-Voigt and IDD-Reuss. The results demonstrate

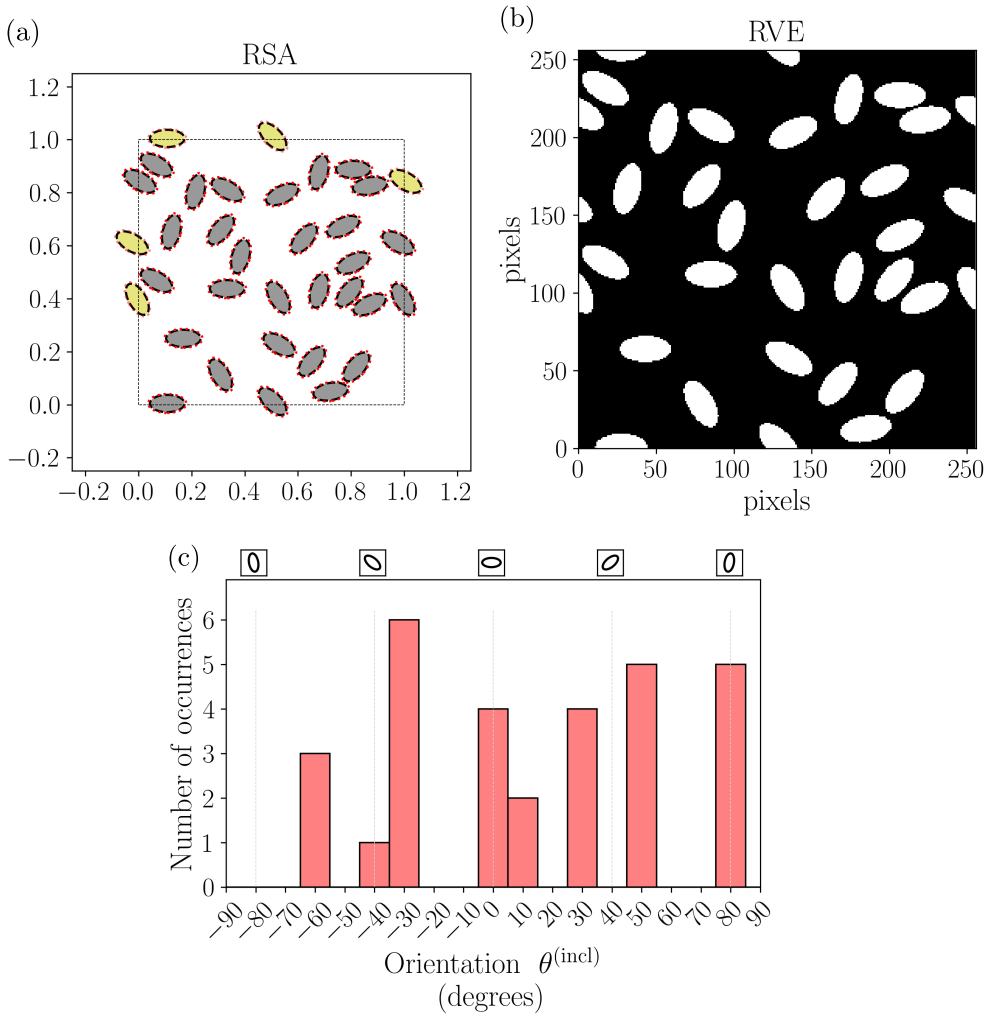

Figure 19: Elliptic inclusions with different orientations: (a) RSA process with RSA-cells coinciding with inclusions. (b) RVE of the microstructure. (c) Number of inclusions per chosen orientation.

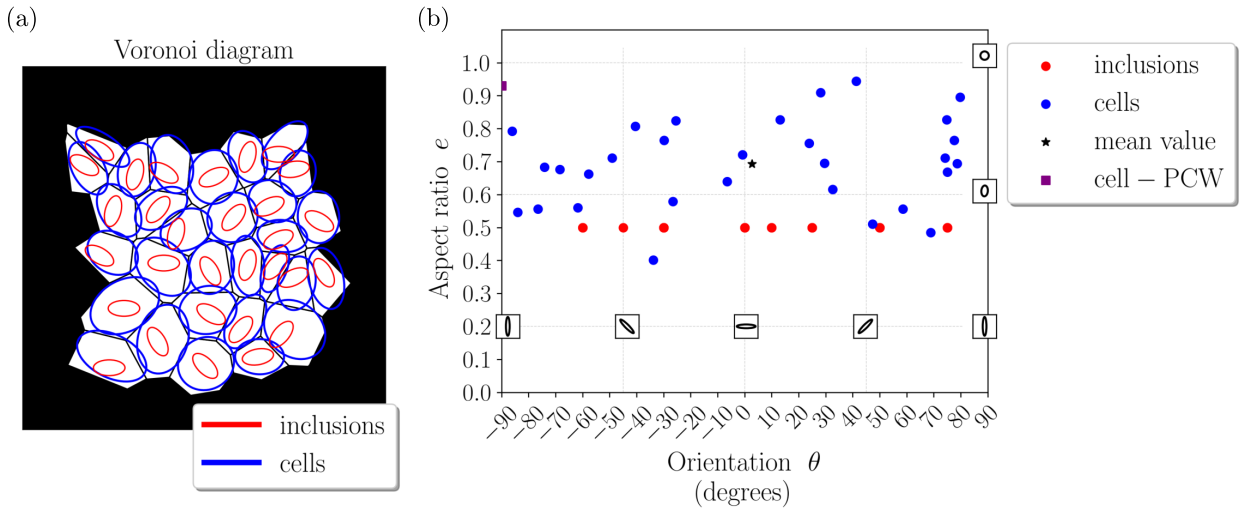

Figure 20: Elliptic inclusions with different orientations: (a) Voronoï diagram, inclusions and respective cells. (b) Scatter plot between aspect ratio and orientation.

that IDD and PCW yield a quantitative improvement compared to MT when compared with the numerical results, except for IDD-Reuss in the evaluation of $k_{\text{eff-II}}$. IDD-Voigt provides the closest results to our benchmark.

5.3.2. Inclusion orientation following the Advani-Tucker law

As a final result to illustrate the relevance of applying IDD and PCW in the 2D effective conductivity context from a microstructure image, we use the Advani-Tucker (AT) law to generate the orientations of the inclusions as depicted in Section 4.1.2. This law is used to simulate the fibers orientation in short-fibers composites in [10, 19] among others. Natural questions are (i) whether and how this orientation distribution may be related to the *spatial* distribution of fibers (both of them being determined by the manufacturing process in actual composites, and by the RSA process in our numerical study); and (ii) if this spatial distribution is worth considering in mean-field estimates.

In this part, as a preliminary investigation, we study the simplified case of composites reinforced by identical ellipses, of aspect ratio 0.5 (*i.e.* much more than actual short fibers), oriented following the AT law. Specifically, in each iteration of the calculation, we fix the parameter m_{AT}, generate the orientations of the inclusions, and pass this information to

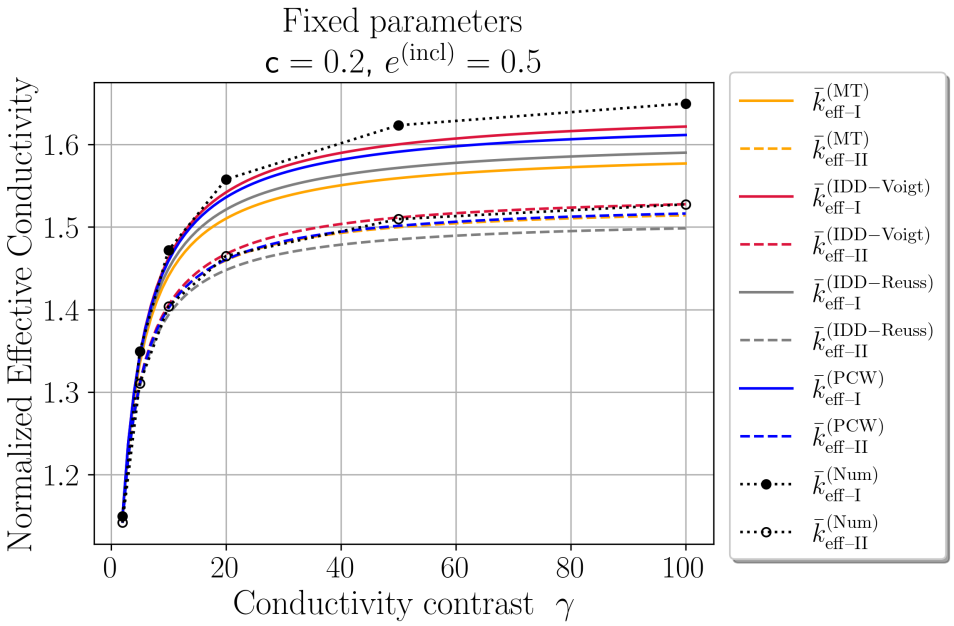

Figure 21: Elliptic inclusions with different orientations: comparison between the different mean-field approaches and the full-field numerical results. The IDD scheme is assisted by double homogenization (see Section 3.1.2).

the RSA algorithm to generate 10 microstructures that are used to calculate the normalized effective conductivity properties. Figure 22 presents four of these RVE for increasing values of m_{AT} (and thus increasing alignment of inclusions).

Figure 23 presents the mean values and standard deviations of the results obtained using the 10 microstructures for each m_{AT} point. A first observation is that the dispersion among the RVE remains moderate, enabling to clearly discriminate models. For the larger conductivity $k_{\text{eff-I}}$, it is observed that IDD and PCW exhibit improved results compared to MT as the m_{AT} parameter increases, *i.e.* as the anisotropy becomes larger. For the lower conductivity $k_{\text{eff-II}}$, all models yield similar results and underestimate the reference value. A transition is observed between the moderate anisotropic configurations ($m_{\text{AT}} \lesssim 5$) where MT estimates are worse to PCW and two-step IDD, and strongly anisotropic configurations ($m_{\text{AT}} \gtrsim 5$) where MT estimates are slightly better. In all cases, the IDD-Voigt method provides the most accurate results among the enhanced models.

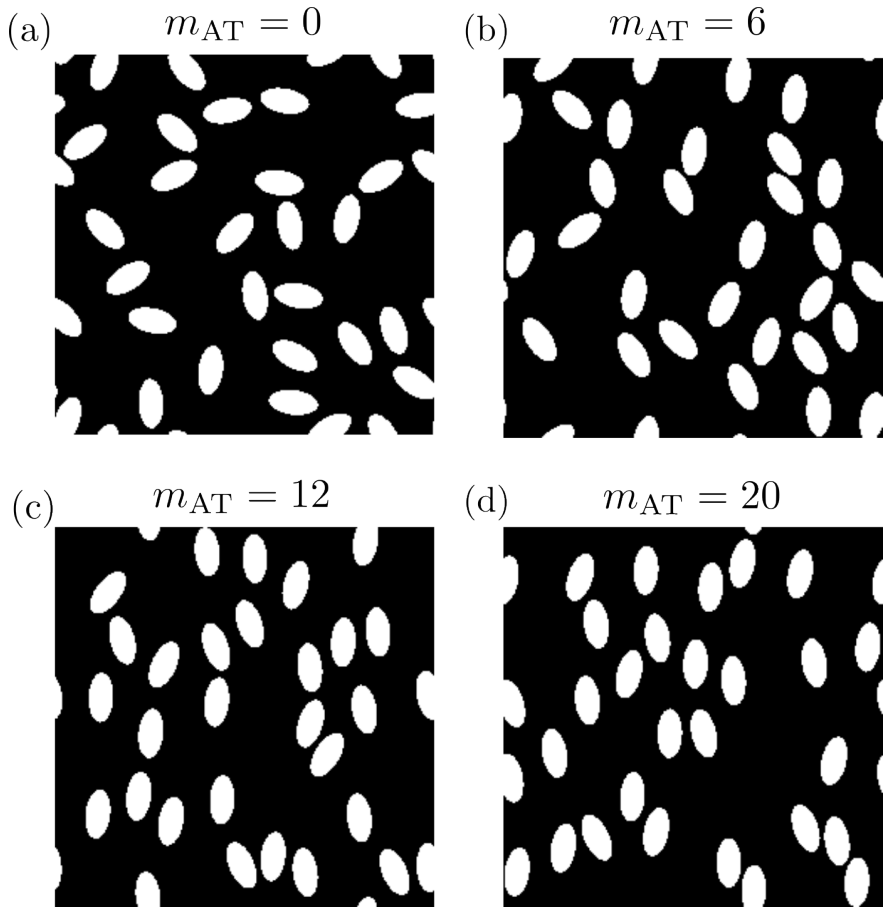

Figure 22: Elliptic inclusions with different orientations following the Advani-Tucker law: examples of RVE for four values of the parameter m_{AT}.

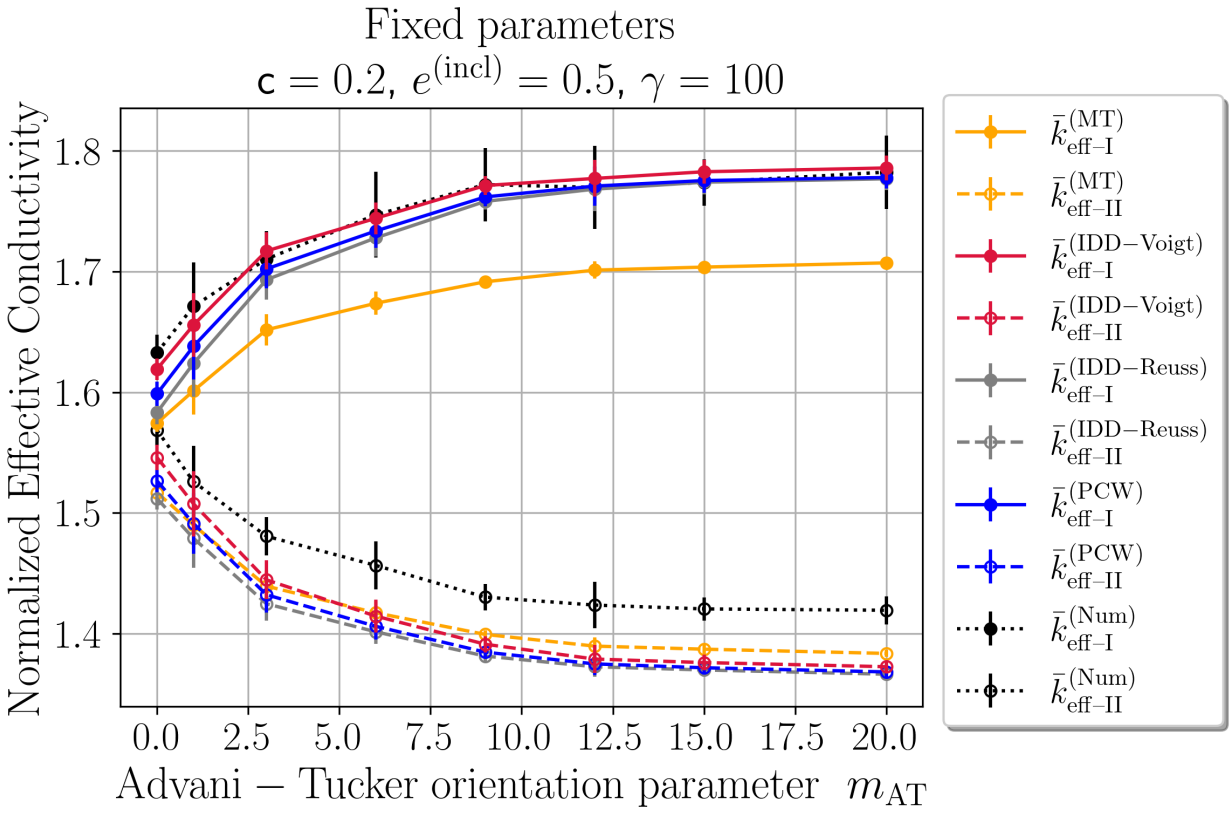

Figure 23: Elliptic inclusions with different orientations following the Advani-Tucker law: mean values and standard deviations of the normalized effective conductivity properties obtained using 10 microstructures for each value of the parameter m_{AT}.

6. Conclusions and perspectives

This study has addressed the utilization of the Interaction Direct Derivative (IDD) and Ponte-Castañeda and Willis (PCW) mean-field models for estimating the effective conductivity properties of composite materials and accounting for the spatial distribution. We determined configurations for which IDD can be applied "as it is" and other where it lacks the major symmetry. In these later cases, two alternative models, namely an IDD-inspired-PCW model (shading a new light on the links between the two models) and a two-step approach, have been proposed. We then described a methodology that employs Voronoï Diagrams to determine the distributional cells needed to parametrize the IDD model. We developed a home-made Python library that integrates homogenization approaches with image processing tools, enabling the semi-analytical process of simulating the fields of interest. We applied this framework to determine the effective behavior of 2D conductive composites and compare the performance of IDD and PCW against the standard Mori and Tanaka (MT) model and the reference FFT-based full-field numerical simulations.

More precisely, artificial RVE were designed to study the influence of spatial distribution on the effective properties for aligned or non-aligned inclusions. In most of the studied cases, the spatial distribution seems to be an important parameter in the sense that IDD model provides qualitatively or quantitively better results than MT. This in particular striking for non-aligned inclusions, see Section 5.3, where no distribution was imposed *a priori*, contrarily to the previous cases, and still IDD-inspired models seemed to capture an information not solely contained in the shapes of inclusions (that would be captured by MT).

These are preliminary results on simplified conductive microstructures. This work needs to be further pursued to consider realistic microstructures, representative of *e.g.* short-fibers composites. At the end, we hope to go beyond the conclusion of [18] that states in the abstract that *"Other models such as the IDD or PCW are of great theoretical importance, but cannot be generally applied for the given material class."*. To do so, the following points should be explored:

1. The extension to 2D and then 3D elasticity should be performed to explore the much

more complex anisotropy issues arising from the higher-order tensor formalism and see if the present conclusions are still applicable. Convenient algorithms to generate Voronoï diagrams are also available in 3D *e.g.* [35].

2. Classical Voronoï diagrams using only the centers of inclusions were used here for simplicity of implementation. In particular, it enabled the use of the same diagram for microstructures made of "pinned" inclusions varying in orientation, volume fraction, and aspect ratio; and therefore to speed up the computation of the effective properties when generating several artificial test cases. To use additively or multiplicatively weighted Voronoï diagrams as discussed in Section 4.2, it would be necessary to determine the properties of the cells for each microstructure. This step may be in particular necessary to address larger aspect ratio of particles, for which classical Voronoï diagram would lead to cells borders intersecting the inclusions.
3. Of course, an important step towards applications to actual composite would be the use of real microstructure images, either 2D for aligned long-fibers or 3D.
4. Finally, a long-term goal is to rely on relevant statistical descriptors of the spatial distribution *e.g.* correlation functions [33] to parametrize these models, rather than image analysis. These descriptors are theoretically linked with the models already, *e.g.* in the original definition of the PCW model using the two-point correlation function of the inclusion phase [14], but were never extracted from an actual microstructure, to the best of our knowledge. An intermediate step would be to generate artificial images given such descriptors, and then apply the presented methodology on these images.

CRediT authorship contribution statement

OLCG: Methodology, Software, Visualization, Formal analysis, Writing – original draft. **RC:** Funding acquisition, Conceptualization, Methodology, Formal analysis, Writing – original draft. **SD:** Methodology, Formal analysis, Writing – review & editing. **RB:** Funding acquisition, Methodology, Formal analysis, Writing – review & editing.

Declaration of competing interest

The authors declare that they have no known competing financial interests or personal relationships that could have appeared to influence the work reported in this paper.

Acknowledgements

Financial support for this project was provided by the Institute of Materials Science (iMAT) of the Alliance Sorbonne Université through a post-doctoral fellowship to OLCG.

Appendix A. Full-field homogenization

Full-field homogenization consists in computing the temperature and flux fields for a basis of elementary macroscopic loads that cover all possible configurations, and then retrieving the effective behavior by computing and relating the means in (3). For conductivity problems, these elementary loads are the unit basis vectors *e.g.* $\langle \boldsymbol{g} \rangle = \mathfrak{e}_j$ if the mean intensity is prescribed. For shorthand notation we regroup them and look for the solution $\boldsymbol{U} = \{U_j\}_{j=1,2}$ of the following problem:

$$\boldsymbol{\nabla} \cdot \boldsymbol{Q}(\boldsymbol{x}) = \boldsymbol{0}, \qquad \boldsymbol{x} \in \mathscr{V}, \tag{A.1a}$$

$$\boldsymbol{Q}(\boldsymbol{x}) = -\boldsymbol{k}(\boldsymbol{x})(\boldsymbol{I} + \boldsymbol{\nabla} \boldsymbol{U}(\boldsymbol{x})), \qquad \boldsymbol{x} \in \mathscr{V}, \tag{A.1b}$$

$$\boldsymbol{U} \text{ is } \mathscr{V}\text{-periodic}, \tag{A.1c}$$

$$\langle \boldsymbol{U} \rangle = \boldsymbol{0}, \tag{A.1d}$$

where $\boldsymbol{I}$ is the second-order identity tensor that regroups the elementary loads: in this problem the total intensity is $\langle \boldsymbol{G} \rangle = \langle \boldsymbol{I} + \boldsymbol{\nabla} \boldsymbol{U} \rangle = \boldsymbol{I}$. This problem is equipped with the local equilibrium equation (A.1a), the local constitutive relation (A.1b), periodic boundary conditions (A.1c), and the usual normalization condition (A.1d) that ensures the uniqueness of the solutions.

The effective conductivity tensor defined by (4) is then found to be:

$$\boldsymbol{k}_{\text{eff}} = \langle \boldsymbol{k}(\boldsymbol{I} + \nabla \boldsymbol{U}) \rangle \,, \tag{A.2}$$

which is proven to be symmetric using reciprocity identities between the uncoupled problems satisfied by the components U_j, that lead to $\langle \boldsymbol{k}\boldsymbol{\nabla}\boldsymbol{U}\rangle_{12} = \langle \boldsymbol{k}\boldsymbol{\nabla}\boldsymbol{U}\rangle_{21}$.

Appendix B. Specific for isotropic phases

565 *Appendix B.1. Normalized expression of the effective properties*

If the phases under study are isotropic, we note $\boldsymbol{k}_\alpha = k_\alpha \boldsymbol{I}$ the conductivity tensor, and the conductivity contrast $\gamma_\alpha = k_\alpha/k_0$ is used to distinguish "more" and "less" conductive inclusions. The effective properties are normalized as well with respect to the conductivity of the matrix k_0, and noted $\bar{\boldsymbol{k}}_{\text{eff}} = \boldsymbol{k}_{\text{eff}}/k_0$. From Table 1 we obtain the normalized estimates:

$$\bar{\boldsymbol{k}}_{\text{eff}}^{(\text{MT})} = \boldsymbol{I} + \sum_{\alpha=1}^{N} \mathsf{c}_\alpha \left(\gamma_\alpha - 1\right) \mathbb{A}_\alpha^{(\text{incl})} \left(\mathsf{c}_0 \boldsymbol{I} + \sum_{\beta=1}^{N} \mathsf{c}_\beta \mathbb{A}_\beta^{(\text{incl})} \right)^{-1}, \tag{B.1a}$$

$$\bar{\boldsymbol{k}}_{\text{eff}}^{(\text{PCW})} = \boldsymbol{I} + \sum_{\alpha=1}^{N} \mathsf{c}_\alpha \left(\gamma_\alpha - 1\right) \mathbb{A}_\alpha^{(\text{incl})} \left(\boldsymbol{I} - \bar{\mathbb{P}}^{(\text{cell})} \sum_{\beta=1}^{N} \mathsf{c}_\beta \left(\gamma_\beta - 1\right) \mathbb{A}_\beta^{(\text{incl})} \right)^{-1}. \tag{B.1b}$$

$$\bar{\boldsymbol{k}}_{\text{eff}}^{(\text{IDD})} = \boldsymbol{I} + \left(\boldsymbol{I} - \sum_{\beta=1}^{N} \mathsf{c}_\beta \left(\gamma_\beta - 1\right) \mathbb{A}_\beta^{(\text{incl})} \bar{\mathbb{P}}_\beta^{(\text{cell})} \right)^{-1} \sum_{\alpha=1}^{N} \mathsf{c}_\alpha \left(\gamma_\alpha - 1\right) \mathbb{A}_\alpha^{(\text{incl})}. \tag{B.1c}$$

expressed in terms of non-dimensional contrasts γ_α and normalized Hill tensors $\bar{\mathbb{P}} := k_0 \mathbb{P}$.

Appendix B.2. Hill and dilute localization tensors

Here we provide the expression of Hill and localization tensors for elliptic inclusions in 2D in an isotropic matrix of conductivity k_0, as given by *e.g.* [22]. Noting $(\mathfrak{a}_1, \mathfrak{a}_2)$ the principal directions of the ellipse, see Figure 14 (a), $a_1 \geq a_2$ the associated semi-axes and $e = \frac{a_2}{a_1} \leq 1$ its aspect ratio, the Hill tensor is given by:

$$\mathbb{P} = \begin{bmatrix} \frac{e}{k_0(1+e)} & 0 \\ 0 & \frac{1}{k_0(1+e)} \end{bmatrix}_{(\mathfrak{a}_1,\mathfrak{a}_2)}. \tag{B.2}$$

Then, from the definition (12), when the constitutive material of the inclusion is also isotropic with conductivity k_α, the dilute localization tensor is:

$$\mathbb{A}_\alpha^{(\text{incl})} = \begin{bmatrix} \frac{k_0(1+e)}{k_0+k_\alpha e} & 0 \\ 0 & \frac{k_0(1+e)}{k_\alpha+k_0 e} \end{bmatrix}_{(\mathfrak{a}_1,\mathfrak{a}_2)} = \begin{bmatrix} \frac{1+e}{1+\gamma_\alpha e} & 0 \\ 0 & \frac{1+e}{\gamma_\alpha+e} \end{bmatrix}_{(\mathfrak{a}_1,\mathfrak{a}_2)}, \tag{B.3}$$

with $\gamma_\alpha = k_\alpha/k_0$ the conductivity contrast. The matrices given in eqs. (B.2) and (B.3) above are the tensors representations in the basis $(\mathfrak{a}_1, \mathfrak{a}_2)$ associated with the ellipse, see Figure 10, and classical rotation operators are applied to obtain their counterpart in the fixed basis $(\mathfrak{e}_1, \mathfrak{e}_2)$.

For circular inclusions, these tensors are isotropic:

$$\mathbb{P}^{(\text{disk})} = \frac{1}{2k_0}\boldsymbol{I} \quad \text{and} \quad \mathbb{A}_\alpha^{(\text{disk})} = \left(\frac{2}{\gamma_\alpha + 1}\right)\boldsymbol{I}. \tag{B.4}$$

Appendix C. Representativity of studied RVE

In this section, the statistical study we did on 10 RVE to ensure their representativity is illustrated by Figures C.24 (for circular inclusions and elliptic RSA cells) and C.25 (for elliptic inclusions and circular RSA cells).

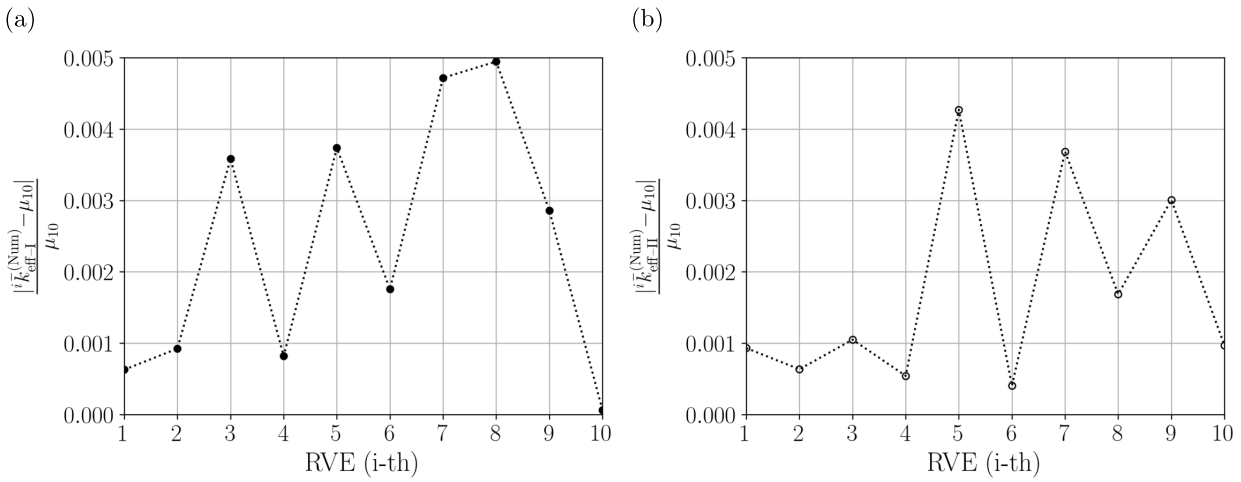

Figure C.24: Elliptic RSA cells and circular inclusions: relative difference between the effective conductivities of 10 RVE (parameters of Table 3) and their means over these 10 RVE, denoted by μ_{10}. (a) $k_{\text{eff-I}}$ and (b) $k_{\text{eff-II}}$.

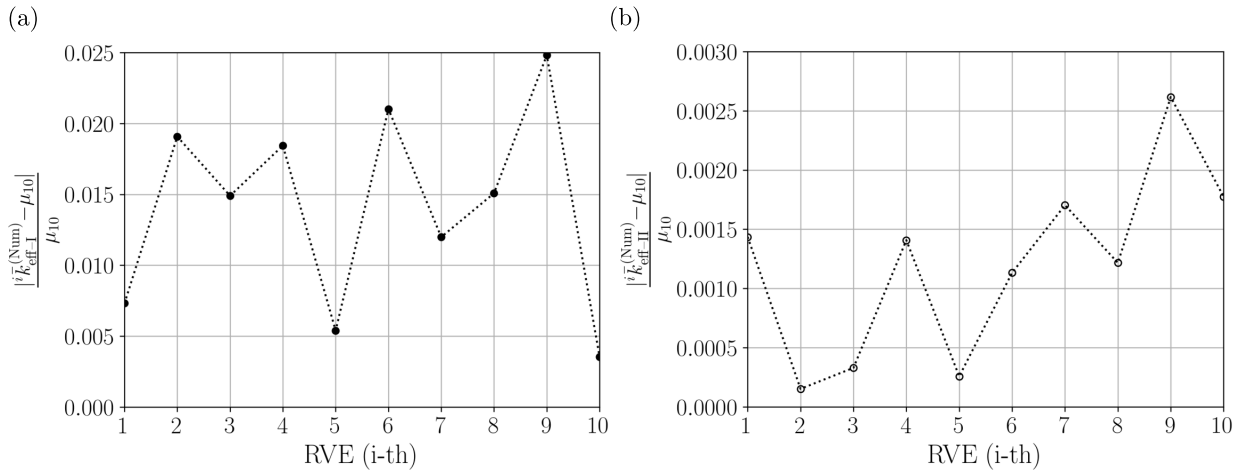

Figure C.25: Circular RSA cells and elliptic identical inclusions: relative difference between the effective conductivities of 10 RVE (parameters of Table 4) and their means over these 10 RVE, denoted by μ_{10}. (a) $k_{\text{eff-I}}$ and (b) $k_{\text{eff-II}}$.

References

[1] M. Z. Khan, S. K. Srivastava, M. Gupta, A state-of-the-art review on particulate wood polymer composites: Processing, properties and applications, Polymer Testing 89 (2020) 106721. doi:10.1016/j.polymertesting.2020.106721.

[2] G. Rajoriya, C. Vijay, P. Ramakrishna, Thermal conductivity estimation of high solid loading particulate composites: A numerical approach, International Journal of Thermal Sciences 127 (2018) 252–265. doi:10.1016/j.ijthermalsci.2018.01.023.

[3] N. Dib, G.-P. Zhil, Generalized modeling of the effective thermal conductivity of particulate composites, Materials Today Communications 27 (2021) 102283. doi:10.1016/j.mtcomm.2021.102283.

[4] J. Bluthé, B. Bary, E. Lemarchand, Contribution of FE and FFT-based methods to the determination of the effective elastic and conduction properties of composite media with flat inclusions and infinite contrast, International Journal of Solids and Structures 216 (2021) 108–122. doi:10.1016/j.ijsolstr.2021.01.007.

[5] M. Schneider, A review of nonlinear FFT-based computational homogenization methods, Acta Mechanica 232 (2021) 1–50. doi:10.1007/s00707-021-02962-1.

[6] S. Lucarini, M. V. Upadhyay, J. Segurado, FFT based approaches in micromechanics: fundamentals, methods and applications, Modelling and Simulation in Materials Science and Engineering 30 (2) (2022) 023002. doi:10.1088/1361-651X/ac34e1.

[7] A. Zaoui, Continuum micromechanics: Survey, Journal of Engineering Mechanics 128 (8) (2002) 808–816. doi:10.1061/(asce)0733-9399(2002)128:8(808).

[8] J. D. Eshelby, The determination of the elastic field of an ellipsoidal inclusion, and related problems, Proceedings of the Royal Society of London. Series A. Mathematical and Physical Sciences 241 (1226) (1957) 376–396. doi:10.1098/rspa.1957.0133.

[9] Q.-S. Zheng, D.-X. Du, An explicit and universally applicable estimate for the effective properties of multiphase composites which accounts for inclusion distribution, Journal of the Mechanics and Physics of Solids 49 (11) (2001) 2765–2788, the Jean-Paul Boehler Memorial Volume. doi:10.1016/S0022-5096(01)00078-3.

[10] B. N. Nguyen, S. K. Bapanapalli, J. D. Holbery, M. T. Smith, V. Kunc, B. J. Frame, J. H. Phelps, C. L. Tucker, Fiber length and orientation in long-fiber injection-molded thermoplastics — part I: modeling of microstructure and elastic properties, Journal of Composite Materials 42 (10) (2008) 1003–1029. doi:10.1177/0021998308088606.

[11] V. Müller, M. Kabel, H. Andrä, T. Böhlke, Homogenization of linear elastic properties of short-fiber reinforced composites – A comparison of mean field and voxel-based methods, International Journal of Solids and Structures 67-68 (2015) 56–70. doi:10.1016/j.ijsolstr.2015.02.030.

[12] T. Mori, K. Tanaka, Average stress in matrix and average elastic energy of materials with misfitting inclusions, Acta Metallurgica 21 (5) (1973) 571–574. doi:10.1016/0001-6160(73)90064-3.

[13] Y. Benveniste, A new approach to the application of Mori-Tanaka's theory in composite materials, Mechanics of Materials 6 (2) (1987) 147–157. doi:10.1016/0167-6636(87)90005-6.

[14] P. Ponte Castañeda, J. Willis, The effect of spatial distribution on the effective behavior of composite materials and cracked media, Journal of the Mechanics and Physics of Solids 43 (12) (1995) 1919–1951. doi:10.1016/0022-5096(95)00058-Q.

[15] M. Hori, S. Nemat-Nasser, Double-inclusion model and overall moduli of multi-phase composites, Mechanics of Materials 14 (3) (1993) 189–206. doi:10.1016/0167-6636(93)90066-z.

[16] D. Du, Q. Zheng, A further exploration of the interaction direct derivative (IDD) estimate for the effective properties of multiphase composites taking into account inclusion distribution, Acta Mechanica 157 (2002) 61–80. doi:10.1007/BF01182155.

[17] L. Charpin, A. Ehrlacher, Estimating the poroelastic properties of cracked materials, Acta Mechanica 225 (9) (2014) 2501–2519. doi:10.1007/s00707-013-1082-0.

[18] P. A. Hessman, F. Welschinger, K. Hornberger, T. Böhlke, On mean field homogenization schemes for short fiber reinforced composites: Unified formulation, application and benchmark, International Journal of Solids and Structures 230-231 (2021) 111141. doi:10.1016/j.ijsolstr.2021.111141.

[19] C. Suarez-Afanador, R. Cornaggia, N. Lahellec, A. Maurel-Pantel, D. Boussaa, H. Moulinec, S. Bordas, Effective thermo-viscoelastic behavior of short fiber reinforced thermo-rheologically simple polymers: An application to high temperature fiber reinforced additive manufacturing, European Journal of Mechanics - A/Solids 96 (2022) 104701. doi:10.1016/j.euromechsol.2022.104701.

[20] O. Pierard, C. Friebel, I. Doghri, Mean-field homogenization of multi-phase thermo-elastic composites: a general framework and its validation, Composites Science and Technology 64 (10) (2004) 1587–1603. doi:10.1016/j.compscitech.2003.11.009.

[21] A. Hussein, B. Kim, Micromechanics based FEM study on the mechanical properties and damage of epoxy reinforced with graphene based nanoplatelets, Composite Structures 215 (2019) 266–277. doi:10.1016/j.compstruct.2019.02.059.

[22] W. J. Parnell, The Eshelby, Hill, moment and concentration tensors for ellipsoidal inhomogeneities in the Newtonian potential problem and linear elastostatics, Journal of Elasticity 125 (2) (2016) 231–294. doi:10.1007/s10659-016-9573-6.

[23] Y. Benveniste, On the effective thermal conductivity of multiphase composites, Zeitschrift für angewandte Mathematik und Physik ZAMP 37 (5) (1986) 696–713. doi:10.1007/BF00947917.

[24] J. Willis, Bounds and self-consistent estimates for the overall properties of anisotropic composites, Journal of the Mechanics and Physics of Solids 25 (3) (1977) 185–202. doi:10.1016/0022-5096(77)90022-9.

[25] H. L. Duan, B. L. Karihaloo, J. Wang, X. Yi, Effective conductivities of heterogeneous media containing multiple inclusions with various spatial distributions, Phys. Rev. B 73 (2006) 174203. doi:10.1103/PhysRevB.73.174203.

[26] F. Deng, Q. Zheng, Interaction models for effective thermal and electric conductivities of carbon nanotube composites, Acta Mechanica Solida Sinica 22 (1) (2009) 1–17. doi:10.1016/S0894-9166(09)60085-9.

[27] A. Aboutajeddine, K. Neale, The double-inclusion model: a new formulation and new estimates, Mechanics of Materials 37 (2-3) (2005) 331–341. doi:10.1016/j.mechmat.2003.08.016.

[28] Y. Zhou, L. J. Sluys, R. Esposito, An improved mean-field homogenization model for the three-dimensional elastic properties of masonry, European Journal of Mechanics - A/Solids 96 (2022) 104721. doi:10.1016/j.euromechsol.2022.104721.

[29] M. Ferrari, Asymmetry and the high concentration limit of the Mori-Tanaka effective medium theory, Mechanics of Materials 11 (3) (1991) 251–256. doi:10.1016/0167-6636(91)90006-L.

[30] Y. Benveniste, G. Dvorak, T. Chen, On diagonal and elastic symmetry of the approximate effective stiffness tensor of heterogeneous media, Journal of the Mechanics and Physics of Solids 39 (7) (1991) 927–946. doi:10.1016/0022-5096(91)90012-D.

[31] C. Kammer, P. P. Castañeda, Variational estimates for the effective properties and field statistics of composites with variable particle interaction strengths, Journal of the Mechanics and Physics of Solids 167 (2022) 104996. doi:10.1016/j.jmps.2022.104996.

[32] W. Tian, L. Qi, M. Fu, Multi-scale and multi-step modeling of thermal conductivities of 3D braided composites, International Journal of Mechanical Sciences 228 (2022) 107466. doi:10.1016/j.ijmecsci.2022.107466.

[33] S. Torquato, Random Heterogeneous Materials, Springer (2nd edition), 2005.

[34] N. Pollmann, F. Larsson, K. Runesson, K. Lundgren, K. Zandi, R. Jnicke, Modeling and computational homogenization of chloride diffusion in three-phase meso-scale concrete, Construction and Building Materials 271 (2021) 121558. doi:10.1016/j.conbuildmat.2020.121558.

[35] H. Moulinec, A simple and fast algorithm for computing discrete Voronoi, Johnson-Mehl or Laguerre diagrams of points, Advances in Engineering Software 170 (2022) 103150. doi:10.1016/j.advengsoft.2022.103150.

[36] M. Bock, A. K. Tyagi, J.-U. Kreft, W. Alt, Generalized Voronoi Tessellation as a Model of Two-dimensional Cell Tissue Dynamics, Bulletin of Mathematical Biology 72 (7) (2010) 1696–1731. doi:10.1007/s11538-009-9498-3.

[37] S. G. Advani, C. L. Tucker, The use of tensors to describe and predict fiber orientation in short fiber composites, Journal of Rheology 31 (8) (1987) 751–784. doi:10.1122/1.549945.

[38] J. K. Bauer, T. Böhlke, On the dependence of orientation averaging mean field homogenization on planar fourth-order fiber orientation tensors, Mechanics of Materials 170 (2022) 104307. doi:10.1016/j.mechmat.2022.104307.

[39] Scikit Image - image processing in Python https://scikit-image.org/.

[40] Scipy - fundamental algorithms for scientific computing in Python https://scipy.org/.

[41] H. Moulinec, P. Suquet, A fast numerical method for computing the linear and nonlinear mechanical properties of composites, Comptes Rendus de l'Académie des sciences. Série II. Mécanique, physique, chimie, astronomie.

[42] H. Moulinec, P. Suquet, A numerical method for computing the overall response of nonlinear composites with complex microstructure, Computer Methods in Applied Mechanics and Engineering 157 (1-2) (1998) 69–94. doi:10.1016/S0045-7825(97)00218-1.